Particle migration and free-surface topography in inclined plane flow of a suspension

By BRIAN D. TIMBERLAKE AND JEFFREY F. MORRIS†

School of Chemical Engineering, Georgia Institute of Technology, Atlanta, GA 30332, USA

Gravity-driven free-surface flow of a suspension of neutrally buoyant particles down an inclined plane channel of constant width has been studied experimentally and by flow modelling. A uniform suspension of spheres, sieved to radii of $a = 53$–$125\,\mu$m or 125–$150\,\mu$m, was introduced to create films of initial depth h_o. The flow was always at small film-depth-based Reynolds numbers. The film depth and the mixture flow profile were measured at the initial and two locations at least $200h_o$ and $400h_o$ downstream. The bulk particle volume fraction, ϕ_B, was varied in the range $0.01 \leqslant \phi_B \leqslant 0.5$; $h_o \approx 1.8$–$3.2\,$mm and the inclination angle relative to horizontal, $0.1° < \alpha \leqslant 90°$, were also varied. Analysis of the particle velocity was performed by stereoscopic imaging to determine particle location followed by particle correlation velocimetry. A two-layer Newtonian viscosity model was applied to the velocimetry results in order to infer particle concentration information. Measured velocity profiles and film depth show that film thickness decreases from h_o, while the velocity gradient at the wall and the mean velocity increase, as the mixture flows down the plane. The free surface, examined using direct imaging, becomes progressively more deformed as α and ϕ_B increase, with the onset of observable deformation found at a particle-scale capillary number of $Ca_p \sim \rho g_x a^2/\sigma = O(10^{-4})$; ρ is the mixture density, $g_x = g \sin \alpha$ is the axial component of gravitational acceleration and σ is the surface tension of the suspending liquid. An existing model for suspension flow which describes phase migration as driven by normal stresses caused by the suspended particles is used to predict the flow, with satisfactory agreement for film depth and development distance for the non-uniform local solid volume fraction, ϕ. The agreement with the detailed ϕ profile is less good, as the model fails to predict the observed $\phi \approx 0$ near the solid boundary while ϕ is overpredicted adjacent to the free surface.

1. Introduction

Free-surface suspension flow appears in diverse contexts including mud flows and bioreactors. This work addresses free-surface film flow of suspensions, with the terminology of film implying a relatively thin layer of suspension. The flow is relevant to processes such as blade coating (Pranckh & Scriven 1990), as it is found in coating with suspensions that the interactions of particles with the surface may affect gloss in paint coatings (Lepoutre & Lord 1990). While the eventual dry film is the quantity of technological interest, the distribution of suspended particles under viscous flow conditions is well-known to be strongly affected by spatially varying shear flow.

† Author to whom correspondence should be addressed; present address: The Benjamin Levich Institute for Physico-chemical Hydrodynamics, City College of New York; New York, NY 10031, USA; morris@ccny.cuny.edu.

Coating flows involving suspensions have, however, received little attention addressing specifically the role particles play in establishing the bulk flow and the form of the surface. The latter issue has been demonstrated to have relevance in recent work by Loimer, Nir & Semiat (2002) illustrating that shear-induced motions of the particles can result in marked deformation of a suspension–air interface. This behaviour reflects particle interactions in the bulk and has no obvious counterpart in pure liquid interfaces. To examine the phenomena involved in a suspension flow with a free surface, we have considered the relatively simple gravity-driven flow down an inclined plane. The goals of the work were to determine for this axially evolving mixture flow the velocity and solids distribution over a range of conditions, as well as to determine the form of the free surface. This work presents both experimental results for this problem and flow modelling employed to aid in their interpretation.

Based upon the similarity of gravity-driven film flow and pressure-driven channel flow, where in the latter a suspension exhibits pronounced particle migration (Koh, Hookham & Leal 1994; Lyon & Leal 1998), migration is expected to play a role in this free-surface flow. A number of suspension flows exhibiting migration have been investigated. Leighton & Acrivos (1987), and later Abbott *et al.* (1991) have shown experimentally that particles will migrate away from regions of high shear to regions of low shear in a viscometric Couette flow of a suspension. Direct observation of the velocity and concentration profile of pressure-driven flow of a suspension in a rectangular channel has been performed using a modified laser-Doppler velocimetry (LDV) method by Shauly *et al.* (1997) (see also Averbakh *et al.* 1997) and by Lyon & Leal (1998). The flows considered in these studies approximated two-dimensional flows across the narrow gap. Particle migration was away from the walls and toward the centre of the channel, leading to the expectation in a gravity-driven film flow of a suspension that neutrally buoyant particles will accumulate adjacent to the free surface.

This expectation does not, however, account for factors arising from the free surface. The most obvious neglected point is that in a free-surface flow, deformation of the interface introduces capillary forces, a type absent in a pressure-driven channel flow. A related point is that the freedom of the interface shape introduces degrees of freedom in the system dynamics, and these have been shown in other geometries, namely a partially filled circular Couette device and a single partially filled rotating cylinder, to be associated with remarkably strong segregation of the particles into concentrated and dilute (or particle-free) bands along the direction perpendicular to the flow. In these flows with rotation about the axis of symmetry, banding is along the axis, and was observed to occur in low-Reynolds-number flow in the partially filled Couette (Tirumkudulu, Tripathi & Acrivos 1999; Timberlake & Morris 2002, 2003) and rimming flow inside a partially filled rotating cylinder (Boote & Thomas 1999; Tirumkudulu, Mileo & Acrivos 2000). These flows involve a free-surface film of suspension flowing due to both device rotation and gravity. The finding of instability of the uniformly mixed state in such flows provides further motivation for examination of suspension flows in free-surface geometries, although it should be noted that no such phenomena are seen in the flow studied here.

The observation of Loimer *et al.* (2002) that the interface with normal in the vorticity direction in a simple-shear flow is strongly deformed suggests that significant stresses drive particle interactions with the free surface. Our investigation considers suspension flow under conditions in which the normal stresses in the suspension are expected to play a role not only at the air–suspension interface, but also in the bulk through particle migration-induced non-uniformity in the solid fraction. Because

capillary normal forces resist the protrusion of particles into the interface driven by bulk shear-induced normal forces, the internal dynamics and surface deformation provide dual demonstrations of the influence of particle normal stresses. This has previously been considered at the bulk scale in work by Zarraga, Hill & Leighton (2000), who addressed the influence of suspended particles upon the bulk normal-stress-induced deformation of the interface in a wide-gap rotating rod geometry. Our consideration of the film flowing down a plane is a rather different geometry, and the vanishing of the average shear rate at the interface in the flow studied here may lead to the expectation that the surface will be unperturbed by the solids. However, this is not the case, as results presented in §3.2 show that small-scale surface deformation about the mean flat film is observable when a capillary number defined $Ca_p = 2\rho g_x a^2/\sigma > 10^{-4}$, with ρg_x the axial driving force due to gravity, a the particle radius, and σ the coefficient of surface tension.

The expectations of particle migration toward the free surface of gravity-driven film flow are derived not only from experiment, but also from a body of work modelling the bulk flow of suspensions. Leighton & Acrivos (1987) proposed a phenomenological model for shear-induced particle flux along gradients in shear, which was developed by Phillips *et al.* (1992) and shown to provide a satisfactory description for a number of flows. Nott & Brady (1994) as well as Morris & Brady (1998) applied a two-fluid type of analysis to show that spatial variation of the suspension normal stresses should play a role in the migration. This framework was further developed by Morris & Boulay (1999), who showed that a consideration of the normal stress differences could account for migration in torsional viscometric flows, and the rheological model proposed in this latter study is employed, in the manner described in §5, for numerical analysis of axial evolution in the film flow.

Previously only a few results from simulation studies of the behaviour of isolated particles or suspensions in film flow with a deformable interface have appeared. Li & Pozrikidis (2002, 2003) have used boundary integral techniques to simulate drops and particles, respectively, in two-dimensional gravity-driven film flow (the particles thus being deformable or rigid disks) down an inclined plane. The results presented by these authors for suspensions of solid particles are limited, but the liquid drops were found to migrate to the centre of the film, i.e. away from both the solid and the free surface. This behaviour differs from the findings for drops in pressure-driven channel flow by Li & Pozrikidis (2000), providing direct (albeit numerical) evidence that the capillary forces from the film interface can have effects upon the phase distribution in mixture film flows.

In order to study the internal bulk dynamics of free-surface flow of a suspension, we use a stereoscopic particle imaging technique. We use direct surface imaging of reflected light to determine the surface topography under various conditions, with power spectral analysis of the images as a characterization tool. The experiments are outlined in the following section. Experimental results are presented for the particle velocimetry and surface reflection studies in §3. The rheological modelling and predictions of the flow are presented with comparison to experimental results in §4.

2. Experiments

2.1. *Suspensions and apparatus*

The suspending fluid used was a mixture of 76% Triton X-100 (t-Octylphenoxy-polyethoxy-ethanol, a surfactant produced by Sigma), 16.2% zinc chloride ($ZnCl_2$),

and 7.8 % water, with the percentages based on mass. This mixture was density-matched ($\rho = 1.180 \, \text{g cm}^{-3}$) and roughly refractive index (RI)-matched to the poly-(methyl methacrylate) (PMMA; Elvacite Company) particles (RI = 1.491 at $T = 20\,^\circ\text{C}$). The suspending liquid viscosity had temperature dependence described by $\eta_0 = 9.13 \exp[-0.12(T-22)] \, \text{Pa s}$, with T in degrees Celsius, based on viscosities at $T = 22\,^\circ\text{C}$–$28\,^\circ\text{C}$ (the range in the laboratory over the period of velocimetry experiments was $T = 22\,^\circ\text{C}$–$29\,^\circ\text{C}$) as measured on a Haake RS600 rheometer. The surface tension of the suspending fluid was $33.5 \, \text{dyn cm}^{-1}$ at $23\,^\circ\text{C}$, measured with a Fisher Surface Tensiometer Model 21.

Suspensions were mixed by first adding the Triton X-100 to the particles and allowing the resulting air bubbles to rise out of the mixture. The $ZnCl_2$ was dissolved in water and the solution was added to the particles and Triton X-100. The suspension was mixed and allowed to cool; cooling was needed as there is apparently a significant heat of mixing for $ZnCl_2$ and water as well as for aqueous $ZnCl_2$ and Triton X-100.

The PMMA particles used in the velocimetry experiments, described in §2.2, were spherical and sieved to radii in the range $a = 125$–$150 \, \mu\text{m}$, and heat treated as described below. The free-surface characterization experiments, described in §2.3, used PMMA particles sieved to a radius range of 53–$125 \, \mu\text{m}$; these particles were not heat treated. The use of different particle sizes was for convenience, as there was a smaller fraction of the larger particles available; an added benefit was that the smaller particles allowed for a thinner film at a given ratio of film depth to particle size, and hence longer flow times (recall velocity scales with the depth squared) before end effects became significant in the short channel used for surface imaging studies. A limited number of the free-surface characterization experiments were performed using PMMA spheres of mean diameter $9.9 \, \mu\text{m}$ and standard deviation of $1.4 \, \mu\text{m}$ (Bangs Laboratories), reported below as of mean radius $\bar{a} = 5.0 \, \mu\text{m}$.

Particles for use in the velocimetry study described in §2.2 must have constant refractive index within the particle, with this refractive index closely matched to the suspending fluid. Improvement of refractive index matching was obtained by the following procedure. Particles were placed for 15 minutes in an oil bath well-mixed by rapid magnetic stirring and heated to $130\,^\circ\text{C}$, and then quenched with dry ice to $-78\,^\circ\text{C}$. The glass transition temperature of PMMA is $125\,^\circ\text{C}$ (Watson 1996). The particles were then resieved, a step needed to remove any which might have become fused. This process greatly improves the clarity of the PMMA particles, allowing visualization through the full depth of a 3 mm film at $\phi_B = 0.4$.

Tracer particles required for the velocimetry technique used here were made from a fraction of the PMMA particles forming the suspension. This fraction was dyed in a hot water bath. Several grams of PMMA particles were placed in a bath consisting of water and black RIT liquid dye. The bath was kept well-mixed while being heated until boiling. The particles were kept under these conditions for approximately two hours to allow diffusion of dye into their surfaces. The mixture was then poured through a sieve to separate the particles from the bath. While the particles were on the sieve, they were washed by flooding with cool water to remove excess dye. Finally the dyed particles were sieved once again to remove fused particles.

Two inclined channels, both constructed from Lexan and 4.4 cm wide but differing in length, were used; one was 183 cm long and the other was 61 cm long. The longer channel was used to examine axial evolution by a velocimetry technique described in §2.2 and characterization of the free surface as described in §2.3; the shorter channel was used only for experiments in which the free-surface deformation was studied.
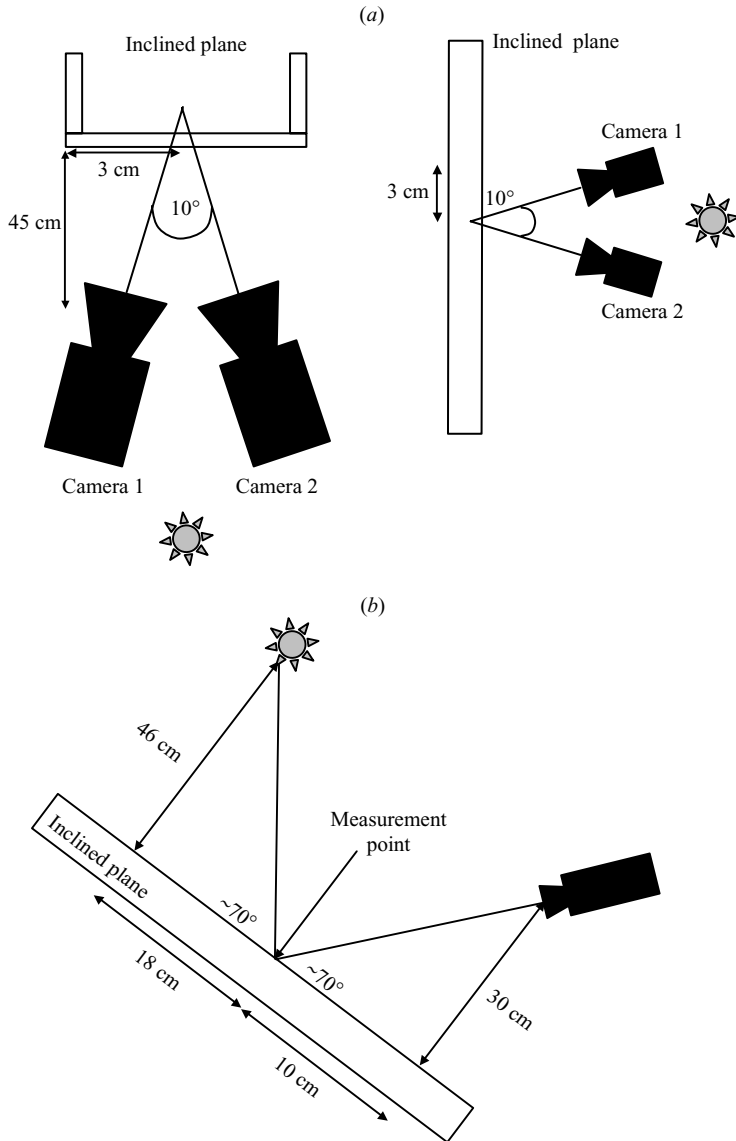
FIGURE 1. Schematics of camera and lighting positions for (*a*) stereoscopic particle imaging velocimetry, and (*b*) free-surface imaging. In (*a*) the flow is normal to the plane of the page in each case.

Digital imaging was used in all experiments described. The cameras used were Ultrak model KC7500CN with Navitar Zoom 7000 Macro Zoom 18–108 mm F/2.5 lenses. Camera positionings used are schematically illustrated in figure 1. Images were captured and sent to computer memory by an IMASYS Falcon Quattro capture card, which is capable of taking images from four NTSC input lines simultaneously. Each image was marked with a time stamp when taken, accurate to one millisecond. For stereoscopic particle positioning, a pair of images is needed at each imaging time; pairs with time stamps differing by greater than 1 ms were discarded, while the time between pairs was 0.5 s or greater. Further details follow below, but it may be helpful

to note that, while this time between images is large relative to many applications, it is appropriate to the system of interest, which has maximum (free-surface) velocities of approximately 0.5–$3\,\mathrm{mm\,s^{-1}}$ (see figures 3 and 5, as well as table 1) and a field of view of 2–$3\,\mathrm{cm}$ on a side.

2.2. *Particle velocimetry*

Stereoscopic particle imaging coupled with a correlation of images at different times has been used to determine the particle velocity within the film. This method is similar to a technique used by Breedveld *et al.* (1998) to determine the self-diffusion of tracer particles within a concentrated suspension in shear flow, and our methodology is here termed 'stereoscopic particle correlation velocimetry', shortened in most cases below to PCV or particle velocimetry. Note that this method differs significantly from stereoscopic 'particle image velocimetry' (PIV) in which particles seed the flow and full-field images at adjacent instants in time are correlated without identification of the particles to obtain full-field velocity information, inclusive of the out-of-plane velocity (Prasad 2000). The well-established PIV technique typically relies on the particles being passive tracers, i.e. having negligible dynamical influence on the flow, and homogeneous seeding (Westerweel 1997). The PCV method used here is designed specifically for the mixture flow, and thus employs tracers which are dynamically identical to the remainder of the suspended particles. Each image contains only relatively few tracers, up to about ten in the typical field of view of 2–$3\,\mathrm{cm}$ on a side, and it should be recalled that these are distributed across the depth of field (here the entire film depth of 2–$3\,\mathrm{mm}$). As a consequence, the method relies on averaging over many images (typically two images per second for about two hours), and does not capture the instantaneous full-field velocity. We are thus not able to report on three-dimensional flow structures or particle clustering. Instead, we consider the mean particle velocity field within the film.

The stereoscopic PCV method consists of three basic steps. First, individual dyed tracer particles are identified in stereoscopic images. Second, their location in a three-dimensional coordinate system is determined by analysis of the image pairs. Third, once all particle positions are known, a correlation between particle positions is made between a given time and the subsequent times, up to a $2\,\mathrm{s}$ separation (for the initial set of positions at $t = 0$, correlation with the positions found at $0.5\,\mathrm{s}$, $1\,\mathrm{s}$, $1.5\,\mathrm{s}$, and $2\,\mathrm{s}$) to determine particle velocity as a function of location in the flow; since a particle may not always be identified, correlation with more than a single subsequent time provides a substantial improvement in the quality of the data. The treatment of all data from an experiment consists of performing the first and second steps on all image pairs to obtain a set of particle locations for each imaging instant, followed by application of the correlation to all images to obtain the velocity data.

2.2.1. *Particle identification*

Particles are identified in the images by first using background subtraction to remove gradients in intensity due to the lighting. Thresholding of the intensity produces a 'binary' image where particles appear black and the background is white. Each group of black points is analysed by an automated computational method to determine if the group represents a spherical particle, implying determination of sufficient circularity in the image. The analysis is based upon constructing ratios of the second, third and

fourth moments ($\mu_{2,3,4}$ respectively) of the groups of points (Li 1992)

$$
\left.
\begin{aligned}
\mu_2 &= \frac{1}{N} \sum_{i=1}^{N} r_i^2 = \frac{1}{\pi R^2} \int_0^{2\pi} \int_0^R r^3 \, \mathrm{d}r \, \mathrm{d}\Theta = \frac{R^2}{2}, \\
\mu_3 &= \frac{1}{N} \sum_{i=1}^{N} r_i^3 = \frac{1}{\pi R^2} \int_0^{2\pi} \int_0^R r^4 \, \mathrm{d}r \, \mathrm{d}\Theta = \frac{2R^3}{5}, \\
\mu_4 &= \frac{1}{N} \sum_{i=1}^{N} r_i^4 = \frac{1}{\pi R^2} \int_0^{2\pi} \int_0^R r^5 \, \mathrm{d}r \, \mathrm{d}\Theta = \frac{R^4}{3},
\end{aligned}
\right\}
\tag{2.1}
$$

where the first equality for each moment is for general shape and the two further equalities are specific to a circle. Here, R is the circle radius and the coordinate system has its origin at the center of mass of the object. Two radius-independent measures are constructed for each object as

$$
\left.
\begin{aligned}
m_1 &= \frac{\mu_3}{\mu_2^{3/2}} = \frac{4\sqrt{2}}{5}, \\
m_2 &= \frac{\mu_4}{\mu_2^2} = \frac{4}{3},
\end{aligned}
\right\}
\tag{2.2}
$$

and again the final equality applies to a circle. If either of the m_i obtained for an object differed significantly from its value for a circle, the object was discarded; in practice, the criterion for this decision was made such that if two spherical particles, of the same size as the particles observed in practice, overlapped by less than 50 % of their projected area, the combined observed object would not be considered a particle and would be discarded. This translates into a 5 % change in m_1 and a 7.5 % change in m_2.

2.2.2. *Stereoscopic particle positioning*

Stereoscopic positioning relies on the fact that the position of an object in space can be determined by observing the object from two different positions. From each camera position, the vector to the object is first determined, and the position of the object in three-dimensional space is given by the intersection of these two vectors. To obtain the necessary information, two cameras were located approximately 45 cm from the inclined plane such that the angles of incidence on the plane of their views were separated by approximately 10°. The distance between the cameras was between 6 and 7 cm; the precise distance is not critical, as the direction is determined separately as described below. The camera positioning relative to the inclined plane is illustrated by the schematic in figure 1(*a*).

The coordinate system in three dimensions is defined by placing an 'optical standard' into the field of view. The optical standard consists of a precision-machined block of aluminium with original dimension 3.5 cm × 2.5 cm × 1.0 cm; one face of this block was further machined to provide five square posts of 400 ± 2 μm on a side. One of the five posts is reduced in height by 2.54 mm (0.100 in.) from the others, which are not reduced in this dimension from the as-received block. In use, the standard is placed with the four long posts in contact with the solid surface of the inclined plane. An image of the face of the optical standard can be seen in figure 2. The posts provide three identifiable points which lie in a plane, against the inclined plane (the fourth of these is not needed), and one identifiable point which lies out of this plane. Designating one of the points as the origin, the positions of all of these points in three-space designated by (x, y, z) are defined, and are noted along with their
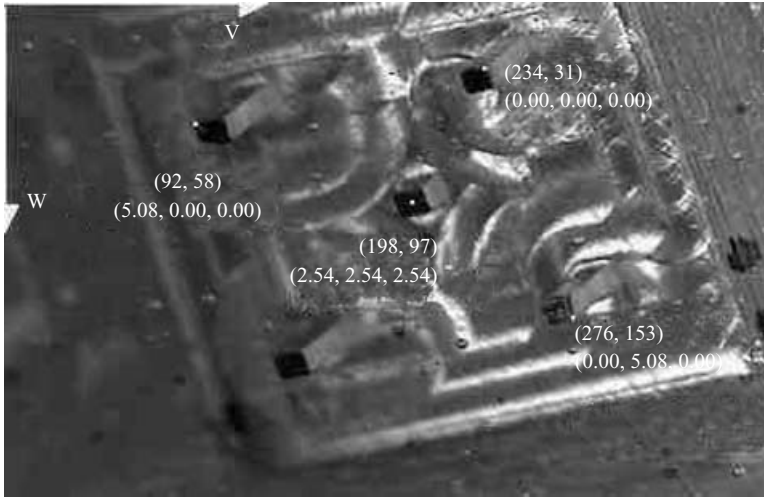
FIGURE 2. Optical standard: the dark squares are the end of the posts of the standard and white dots on these are positions of critical features used in defining the transformation from image space to physical space. These positions are labelled in pixels (V, W) (upper text) and three-dimensional physical position (x, y, z) referenced to the uppermost identified point in the picture (lower text).

pixel location (V, W) in the figure. Knowledge of these four positions on the optical standard allows us to define a transformation from a point in an image to a position vector in three-dimensional physical space, i.e. $T : (V, W) \rightarrow (x, y, z)$. The details of the development of the transformation are provided in the Appendix.

In the analysis, the assumption is made that all vectors from the camera to the measurement volume are parallel to the focal axis, and this is validated experimentally. The optical standard was first used to define the transformation from image to physical space. The optical standard was then moved a known distance and the locations of the features were calculated and compared to their actual positions. The distances of interest are of the order of the film thickness, typically $h_o = 2$–3 mm, and when the optical standard was moved 2 mm with a micrometer driven linear translator (MVN-80; Newport) in both the vertical and horizontal directions, the error in the position of the features was less than 40 µm in each of the three directions, with the largest error in the vertical.

2.2.3. *Correlation velocimetry*

Particle velocities are determined by first finding the vector between each particle at time t and each particle at time $t + \Delta t$, $(\Delta x)_{ij} = x_j(t + \Delta t) - x_i(t)$ for i and j labelling all particles at t and $t + \Delta t$, respectively; recall that $\Delta t = 0.5$–2 s. Velocities are determined as $v = (\Delta x)_{ij}/\Delta t$. Each velocity is assigned to the position at the mid-point between the two particle positions used to create it. The v are assigned to bins according to distance from the solid surface, z, and then are further classified into bins according to magnitude in the x-, y-, and z-directions. We assume that there is no correlation between a given particle at time t and a particle at time $t + \Delta t$ which lies upstream (at smaller x), so that the distribution of negative x-directed velocities represents part of the expected uncorrelated distribution of velocities associated with unlike particles for a given position box. The number of velocities which lie in each velocity box is totalled and the number found with a negative v_x is subtracted from
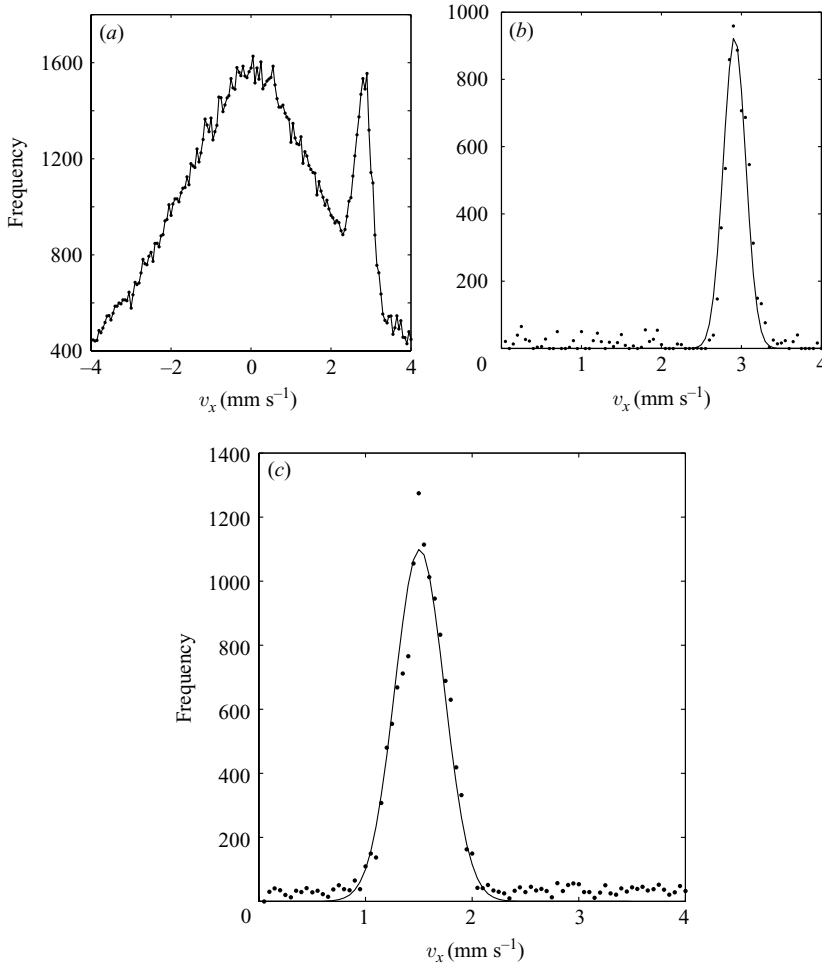
FIGURE 3. Velocimetry data. (*a*) Raw velocity frequency data for tracer particles ($\phi_B = 0.005$) for the box centred 2.6 mm above the solid surface of the inclined plane where $h_o = 3.2$ mm and $\alpha = 33.5°$. Gaussian fit of correlated velocity frequency data for (*b*) tracer particles ($\phi_B = 0.005$) for the velocity box centred 2.6 mm above the solid surface of the inclined plane where $h_o = 3.2$ mm and $\alpha = 33.5°$ and (*c*) $\phi_B = 0.3$, $\alpha = 60.8°$, $h_o = 2.72$ mm, and $x = 15$ cm for the velocity box centred 1.4 mm above the solid surface of the inclined plane.

the number in the box with the corresponding positive v_x of the same magnitude. This process leaves only the correlated velocity information. Only positive velocities were retained from this operation, with the result that the noise seen in figure 3 is strictly positive, but this is not found to affect the desired information, i.e. the value of velocity occurring with greatest frequency.

The raw velocity data for the tracer study at $z = 2.6$ mm can be seen in figure 3(*a*) and the correlated data for this same location is shown in figure 3(*b*). A best fit Gaussian curve is determined for the velocity data for the bin at each distance above the solid surface, as illustrated in figure 3(*b*), with the velocity taken as the mean of the Gaussian. The procedure was found to apply well to concentrated suspensions, up to $\phi_B = 0.4$, with a qualitatively similar fit to that found for the tracer in figure 3(*b*) seen in the $\phi_B = 0.3$ data in figure 3(*c*).
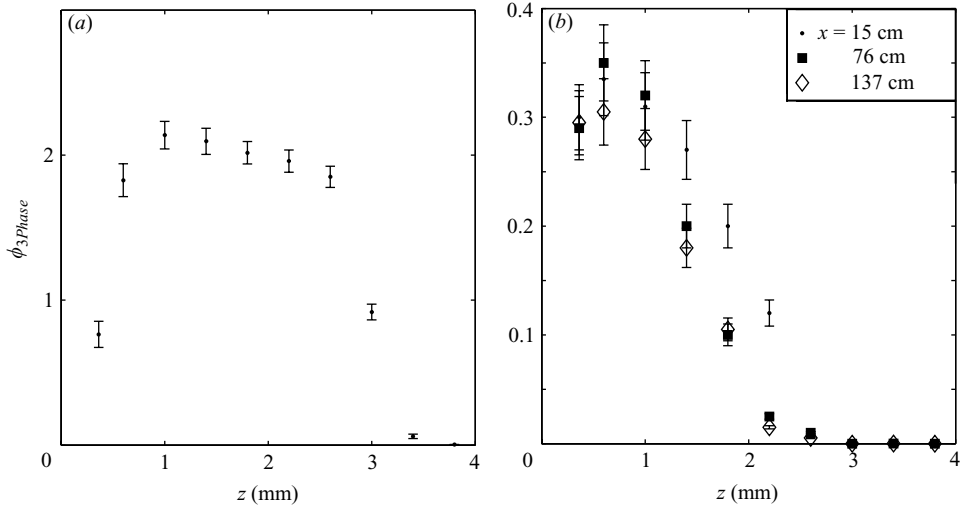
FIGURE 4. Concentration profiles from direct counting of particles in (*a*) a tracer experiment ($\phi_B = 2 \times 10^{-4}$, $2a = 250\,\mu m$, $h_o = 2.8\,mm$, $\alpha = 33.5°$) and (*b*) $\phi_B = 0.3$, $2a = 250\,\mu m$, $h_o = 1.8\,mm$, $\alpha = 60.8°$. Here ϕ_{3Phase} represents the particle fraction in the full system which consists of liquid, gas, and particles. This arises because of the unknown instantaneous location of the free surface.

The local particle fraction profile $\phi(z)$ is also of interest. While in principle accessible using the image data used for the particle correlation velocimetry (PCV), particle fraction was only reliably determined from the detected particle positions for dilute conditions. Recall that images were taken through the solid surface. Although we were able to visualize through the entire film, we found that the probability of detecting a dyed particle near the solid surface was greater than the probability closer to the free surface. If the probabilities were equal, $\phi(z)$ could be determined as proportional to the number of particles counted within a volume. The results from a tracer study at $\phi_B = 2 \times 10^{-4}$, shown in figure 4(*a*), along with the results from an experiment done with $\phi_B = 0.3$, shown in figure 4(*b*), indicate a detection bias depending on the distance of the particle from the lower boundary of the film. The concentration profile for $\phi_B = 0.3$ is, in fact, inconsistent with the velocity data taken for those experiments, as the shear rates found from the velocity profile do not agree with the effective viscosities implied by the particle concentrations shown in figure 4(*b*). The velocity data are not subject to the same detection bias as the concentration, as equal probability of detecting a particle at the different positions is not required. It is most likely that the failure of the method for determining the detailed particle fraction is due to insufficiently close matching of the refractive indices of particles and fluid.

Rather than using direct particle position sampling to assess the particle concentration, we resorted to treating the flow as consisting of two layers with different Newtonian viscosities. The choice of only two layers is described below. Fitting of the experimentally determined velocities to a two-layer model provides indirect information on particle concentration inhomogeneity when combined with an empirical relation between ϕ and effective viscosity; the specific viscosity model used in treating the data is given in §3. This two-layer model yields a three-parameter model of the
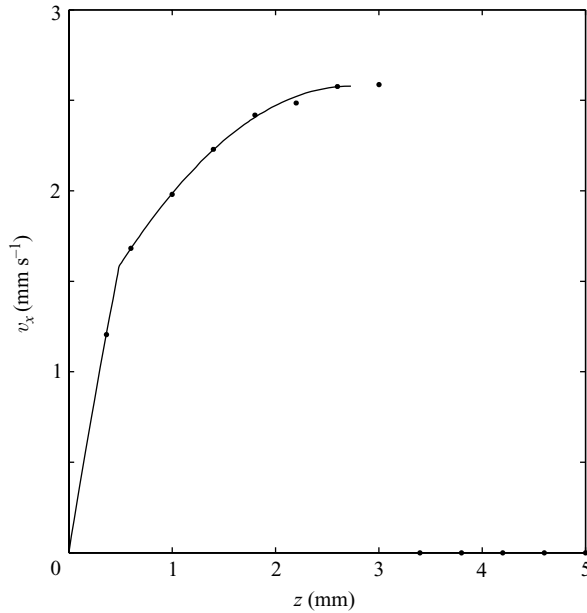
FIGURE 5. Velocities determined experimentally and the two-layer Newtonian viscosity model fit for $\phi_B = 0.3$, $\alpha = 60.8°$, $h_o = 3.21$ mm, and $x = 137$ cm. The model parameters are $\eta_{s_1} = 7.81$ Pa s, $\eta_{s_2} = 25.8$ Pa s, and $\beta = 0.82$.

velocity,

$$
\left.
\begin{aligned}
v(z) &= \frac{h^2 \rho g_x}{2} \left[\frac{1 - \beta^2}{\eta_{s_1}} + \frac{\beta^2 - (h - z)/h^2}{\eta_{s_2}} \right] \quad \text{for} \quad z \in [(1 - \beta)h, h], \\
v(z) &= \frac{h^2 \rho g_x}{2} \left[\frac{1 - (h - z)/h^2}{\eta_{s_1}} \right] \qquad\qquad \text{for} \quad z \in [0, (1 - \beta)h],
\end{aligned}
\right\}
\tag{2.3}
$$

where $g_x = g \sin \alpha$. The parameters of the model are the viscosities (η_{s_i}) of the fluid layers as well as the location of the boundary between the two distinct layers, βh. The variable β is confined to the interval between 0 and 1, and represents the fraction of the film at the measurement position made up of the layer of viscosity η_{s_2} next to the free surface. The model fit to measured velocity data is made by minimizing the squared error between the model velocity and the actual velocity data using a Nelder–Mead simplex method (Nelder & Mead 1965). A typical two-layer Newtonian viscosity fit is shown in figure 5. Uncertainty in the location of the separation between the two layers within this model is ultimately related to positioning error of particles in z, which is greater than the absolute precision of the measurement location technique, previously noted to be good to about 40 μm. The location uncertainty is due to the fact that association of a given particle with the wrong bin results in a shift by the bin size in its position used in the data treatment. Since only a fraction less than one-half of the particles associated with a bin are expected to be subject to this uncertainty, we estimate an upper bound on the uncertainty in the location of the division between layers to be one-half of the bin size, i.e. about $\delta z/2 = 200$ μm. This corresponds to an uncertainty in the dimensionless β of $\delta z/2h$, and this is reported in table 1, below.

From the implied viscosity and the relationship between particle fraction and effective viscosity, $\eta_s(\phi)$, we determine the implied particle fraction in each layer. The suspending liquid viscosity is determined for each experiment by fitting a one-viscosity

model to the velocity profile taken nearest the start of the channel, assuming ϕ is uniform at the bulk concentration across the film. The assumptions are apparently justified: table 1 shows that the viscosities from the two-viscosity fit for the pure fluid (experiment 1) are almost identical to those of the one-viscosity fit, while the two viscosities for the suspension at the earliest measuring location, $x = 15$ cm, were found to be relatively close in value, 8.0 and 8.1 Pa s. The pure fluid viscosity is determined in this manner because of its sensitivity to temperature, which varied from one experiment to another. The depth of the film at $x = 15$ cm is taken as h_o, although some of the early evolution has presumably taken place by this point.

While it is tempting to represent the flow as more than two Newtonian liquid layers, there is insufficient velocity data to warrant this. Typically, our velocity profiles are made up of 5 to 9 data points, and a three-viscosity model requires five model parameters. A fit with five parameters with only five data points introduces excessive sensitivity, where small changes in the measured data produce large changes in the predicted values. Given this lack of velocity data, the most we can safely extract from a model of this type is two viscosities, along with the location where the effective viscosity changes.

2.3. *Free-surface characterization*

In order to characterize the deformation in the free surface of inclined-plane flow, a series of images is taken of the reflection of light from the free surface. A camera is placed above the free surface such that its focal axis creates an angle of approximately 70° from the film (or 20° from the mean surface normal, $\langle n \rangle \approx e_z$ where e_z is the unit vector in z), as shown in figure 1(*b*). Lighting is by a 300 W white light bulb without diffuser, providing an approximate point source with the light reflected from the undisturbed flat interface reaching the centre of the frame of the camera. If the surface is deformed such that the local surface normal, $n(x, y)$, is in a direction sufficiently different from the mean normal, light is reflected away from the camera producing a dark region in the image.

The series of intensity images was subjected to Fourier analysis to obtain length scale information about the free surface. Both one- and two-dimensional transforms were considered, and the power spectral density (PSD) determined for each.

One-dimensional PSDs were constructed in both the flow and spanwise directions. The one-dimensional PSD is obtained by first dividing each image into individual data sets. Each row of pixels in each image was treated as an individual data set for determining the mean PSD in the spanwise direction and each column of pixels is treated as an individual data set for determining the mean PSD in the flow direction.

The first step in determining the PSD of an individual data set is to take the fast Fourier transform (FFT) of the image intensity data (essentially brightness) with the mean intensity subtracted. The power contained within each wavenumber band for the specific data set is then determined from these Fourier coefficients. The normalized power is defined as

$$P(k) = \frac{M(k)M(k)^*}{\max_{b=1}^{N}\{M(b)M(b)^*\}}, \quad (2.4)$$

where $M(k)$ is the vector of Fourier coefficients and $*$ denotes the complex conjugate. The mean PSD in the spanwise direction is simply the mean of the spanwise PSDs

determined for all data sets in the series

$$\overline{P}(k) = \frac{1}{S} \sum_{b=1}^{S} P_b(k) \qquad (2.5)$$

where $\overline{P}$ is the mean PSD, and S is the number of data sets in all images. The same process is used to determine the mean PSD in the flow direction. This method is similar to one of the methods used in Loimer *et al.* (2002), although we have used the full field of the image rather than a narrow band from the image.

A two-dimensional Fourier analysis was also considered. The first step in this process is to take the two-dimensional FFT of the raw image, again after subtracting the mean intensity. A two-dimensional PSD is constructed for each image in the series, with normalization by the largest power,

$$P(j, k) = \frac{M(j, k)M(j, k)^*}{\max_{b=1, c=1}^{N_1, N_2}\{M(b, c)M(b, c)^*\}}, \qquad (2.6)$$

where $M(j, k)$ is the array of Fourier coefficients, N_1 is the number of pixel rows, and N_2 is the number of pixel columns. The reported result for a given experiment is the mean of the two-dimensional PSDs over all images,

$$\overline{P}(j, k) = \frac{1}{S} \sum_{b=1}^{S} P_b(j, k). \qquad (2.7)$$

Here S represents the number of individual images in the series.

3. Experimental results

The specific aims of this work were to measure the flow of a non-colloidal suspension in free-surface film flow in Stokes flow, and to determine the form of the free surface under such flow conditions. Neglect of inertia is justified as the film Reynolds number satisfied

$$Re_f = \frac{\rho u_{\max} h_o}{\eta_{s_o}} \sim \frac{\rho^2 g_x h_o^3}{\eta_{s_o}^2} < 0.01$$

for all experiments in this study, where we recall that ρ is the mixture density, $g_x = g \sin \alpha$ is the axial component of gravity, h_o is the initial film thickness, $u_{\max}$ is the maximum observed velocity, and η_{s_o} is here the dimensional effective viscosity of a suspension with a particle concentration equal to ϕ_B. The effective viscosity is modelled by the empirical form

$$\eta_s(\phi) = \eta_0 \left(1 - \frac{\phi}{\phi_{\max}}\right)^{-2},$$

where η_0 is the suspending liquid viscosity, and the maximum packing fraction is taken as $\phi_{\max} = 0.65$. The particle-scale Reynolds number is much smaller,

$$Re_p = \frac{\rho \dot{\gamma} a^2}{\eta_0} < 10^{-5},$$

where a is the particle radius, and the representative shear rate is given by the film average value of $\dot{\gamma} = u_{\max}/h_o$.

As in prior experimental examinations of suspension flows with varying shear rate (Leighton & Acrivos 1987; Abbott *et al.* 1991; Lyon & Leal 1998) and predicted by

theoretical treatments (Phillips *et al.* 1992; Nott & Brady 1994; Morris & Boulay 1999) when applied to rectilinear flows, we observe the migration of particles away from regions of high shear at the wall toward the low-shear-rate region closer to the free surface. We are, however, unable to make precise statements about the solids fraction close to the free surface based upon our results. We have also observed the deformation of a free surface caused by particle interactions in the bulk (subsurface) flow which has been previously observed by Loimer *et al.* (2002). Note that the surfaces in the work of Loimer *et al.* had normal along the vorticity direction of a band-driven simple shear, and thus the fluid adjacent to (just below) the free surface was not shear stress free as in the case of the surfaces studied here. It is thus interesting to note the relative similarity of the observations.

3.1. *Particle velocimetry*

In order to analyse the results and facilitate comparison between different experiments, the coordinates are scaled with h_o, taken as the film depth 15 cm downstream from the introduction of suspension to the channel. All velocities reported here have been scaled by U_0; this is the surface velocity of a parabolic Newtonian flow having the same depth and same axial flux as the suspension at the initial measurement location, and varies over the range 0.5–3 mm s^{-1} in the reported experiments. The scaled flows presented for all conditions are thus equivalent on a dimensionless flux basis to that of the reference parabolic flow. The actual velocities from the experiments can be recovered from the scaled velocities plotted by using the values of U_0 from table 1. We note that only small (1–5 %) variations in axial flux, apparently resulting from experimental uncertainty, were observed in integration of the profiles.

The velocity profile evolution is illustrated by figure 6, which shows the measured velocities at the three measurement locations for suspensions of $\phi_B = 0.2$, 0.3, and 0.4. Note that the measured velocity profiles at 15 cm are very nearly equivalent to the parabolic form of a Newtonian fluid for $\phi_B = 0.2$ and 0.3, while for $\phi_B = 0.4$ the shear rate at the wall at this location is actually below the Newtonian result, indicating that we are not able to observe significant influence of migration at this point. We thus take h_o from measurements at this location. As the fluid moves down the inclined plane, the velocity at the measurement locations nearest the wall is observed to increase, e.g. by a factor of about two for $\phi_B = 0.2$. The cases displayed have films $2.3 < h_o < 2.9$ mm. While the angle of inclination differs for the $\phi_B = 0.3$ case, results which follow below show this change in angle has little or no discernible effect upon the scaled velocity profiles. In figure 6(*b*), the small change seen for $\phi_B = 0.3$ between the profiles measured at $x = 76$ cm and $x = 137$ cm indicates nearly full development for this volume fraction, although without the ability to take data further downstream (the device being too short to allow this) we cannot say this with certainty. The essentially negligible differences for $\phi_B = 0.4$ at these locations indicate fairly certainly that the final measurements for this solids fraction are fully developed. Significant difference is seen between these axial locations for $\phi_B = 0.2$, and thus this condition is probably not fully developed at the final station. The modelling described in §4 predicts that the velocity profile for $\phi_B = 0.2$ at $x = 137$ cm ($x/h_o \doteq 520$ in experiment 2) will not be fully developed, while the predictions for $\phi_B = 0.3$ and 0.4 suggest complete evolution before the final measurement location.

Figure 7 shows results from a number of experiments, all at $x = 137$ cm from the onset of flow. In part (*a*), although the $\phi_B = 0.2$ flow may not be fully developed, the scaled velocity profiles have generally similar form, with the suspensions invariably shearing much more rapidly near the wall than the Newtonian fluid having the same
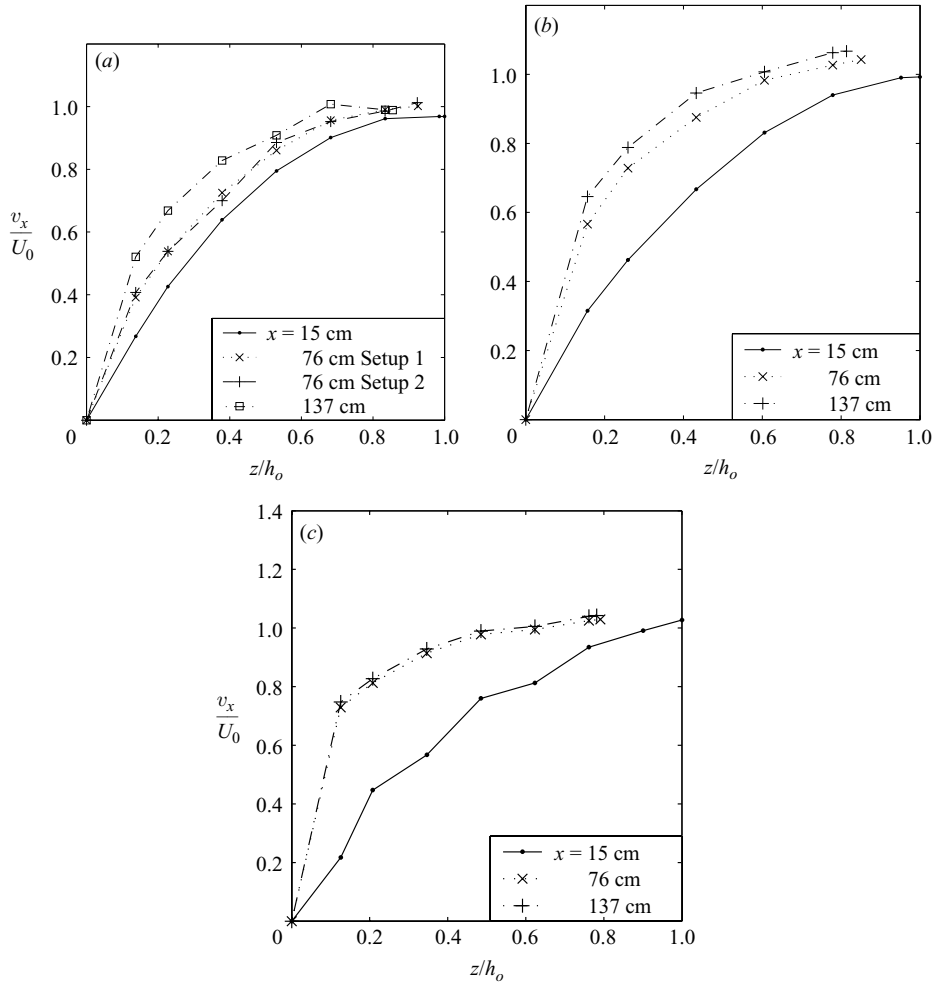
FIGURE 6. Measured velocity at three axial locations is shown for (*a*) $\phi_B = 0.2$, $\alpha = 33.5°$, and $h_o = 2.6$ mm; (*b*) $\phi_B = 0.3$, $\alpha = 60.8°$, and $h_o = 2.3$ mm; and (*c*) $\phi_B = 0.4$, $\alpha = 33.5°$, and $h_o = 2.9$ mm.

axial flux. Considering the detailed forms, the scaled velocities for $\phi_B = 0.3$ and 0.4 are very similar. The profile for $\phi_B = 0.2$ is closer in form to the parabolic flow of a Newtonian fluid (shown for reference), although substantial influence of migration is nonetheless evident. Specifically, migration away from the solid surface reduces the effective viscosity in this portion of the flow, and thus results in more rapid shearing near the wall and blunting of the velocity away from the solid surface. There is a consequent reduction in the film thickness to satisfy the mass flux requirement, as the higher velocities caused by more rapid shearing at the wall integrate to the imposed flux over a thinner film. Figure 7(*b*) shows that the depth of the film has little impact upon the scaled form of the velocities just measured, and figure 7(*c, d*) together show that this is true also of the angle. This agrees with expectations derived from Stokes suspension flow in channels, in that the evolution of the flow depends primarily upon the strain undergone by the material rather than the rate of strain.

The large velocity gradient near the wall, shown in figures 6 and 7, implies that the particle concentration near the wall has become nearly zero in the fully developed
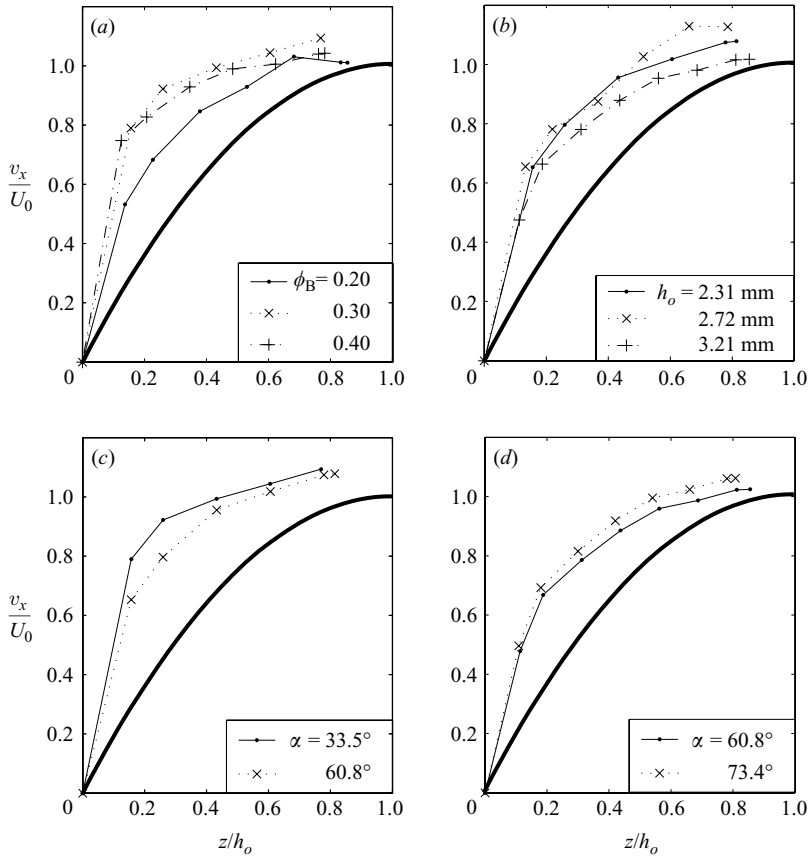
FIGURE 7. Comparison of velocity profiles normalized to the same axial flux, measured at $x = 137$ cm for various conditions: (a) $\phi_B = 0.2$, 0.3, and 0.4 for $\alpha = 33.5°$, and $h_o = 2.64$ mm, $h_o = 2.31$ mm, and $h_o = 2.89$ mm respectively; (b) varying h_o for $\phi_B = 0.3$, and $\alpha = 60.8°$; and varying α for $\phi_B = 0.3$ for (c) $h_o = 2.3$ mm and (d) $h_o \approx 3.3$ mm. The heavy line in each case represents the Newtonian fluid parabolic profile of the same axial flux.

state. Note that in channel flow experiments, Lyon & Leal (1998) also saw a sharp decrease in ϕ at the walls, as did Nott & Brady (1994) in simulations of this flow.

Results for all experiments for which film depth was measured are presented in table 1. All experiments involving concentrated suspensions resulted in downstream velocity profiles which exhibited an increase in the velocity gradient near the wall. Implied viscosities determined from a two-layer Newtonian viscosity model and implied particle fractions are presented. Implied particle fractions were determined by solving for ϕ from the empirical effective viscosity relation noted previously,

$$\eta_{s_i} = \eta_0 \left(1 - \frac{\phi}{\phi_{max}} \right)^{-2},$$

where η_{s_i} with $i = 1$ or 2 is a layer viscosity from the two-layer Newtonian viscosity model, η_0 is the pure fluid viscosity, and $\phi_{max} = 0.65$. Particle flux matching from the two-layer model to the experimentally set value was within 15 % in all cases. This seemingly large uncertainty is due to uncertainty in the location of the boundary between layers within the two-layer model.

Exp.	ϕ_B	α deg.	Q mL min⁻¹	x cm	h mm	U_0 mm s⁻¹	η_{s_1} Pa s	η_{s_2} Pa s	β	ϕ_1	ϕ_2	η_0 Pa s
1	0	33.5	13.39	76	2.68	2.74	8.0	8.1	0.88 ± 0.07	0.00	0.00	8.1
2	0.2	33.5	13.39	15	2.64	2.71	7.7	8.1	0.54 ± 0.08	0.19	0.20	3.9
				76	2.44		4.8	8.4	0.83 ± 0.08	0.07	0.21	
				76	2.44		4.6	8.2	0.86 ± 0.08	0.05	0.20	
				137	2.26		3.3	9.6	0.81 ± 0.09	0.00	0.24	
3	0.3	33.5	5.68	15	2.31	1.29	12.1	15.6	0.57 ± 0.09	0.29	0.33	3.7
				76	1.89		5.1	16.0	0.76 ± 0.11	0.09	0.34	
				137	1.78		3.7	19.1	0.78 ± 0.11	0.00	0.36	
4	0.3	60.8	5.68	15	2.31	1.34	18.0	19.9	0.86 ± 0.09	0.29	0.31	5.6
				76	1.97		8.2	20.7	0.79 ± 0.10	0.11	0.31	
				137	1.88		6.9	20.8	0.79 ± 0.11	0.06	0.31	
5	0.3	60.8	9.52	15	2.72	1.87	20.0	17.5	0.63 ± 0.08	0.31	0.28	5.6
				76	2.34		8.5	20.5	0.83 ± 0.09	0.13	0.31	
				137	2.14		6.2	17.9	0.83 ± 0.10	0.04	0.29	
6	0.3	60.8	14.30	15	3.21	2.43	21.3	19.4	0.60 ± 0.06	0.30	0.29	6.0
				76	2.80		8.5	25.0	0.83 ± 0.07	0.10	0.33	
				137	2.74		7.8	25.8	0.82 ± 0.08	0.08	0.34	
7	0.3	73.4	17.61	15	3.33	2.95	19.5	20.6	0.90 ± 0.06	0.29	0.30	5.9
				137	2.69		6.7	21.5	0.82 ± 0.08	0.04	0.31	
8	0.4	33.5	2.78	15	2.89	0.53	45.5	48.3	0.94 ± 0.06	0.40	0.41	6.5
				76	2.28		8.3	73.1	0.90 ± 0.09	0.08	0.46	
				137	2.26		7.6	72.2	0.91 ± 0.09	0.05	0.46	

TABLE 1. Results from all velocimetry experiments discussed. Left to right in the first five columns are the experiment number, bulk particle volume fraction, angle of inclination from horizontal, the imposed volumetric flux, and axial position of the measurements. The film depth determined is h, while the maximum (surface) velocity of the Newtonian film flow (having flux Q and the viscosity of uniform suspension at ϕ_B) is labelled U_0. The parameters η_{s_1}, η_{s_2} and β are the results of a fit of the experimental results to the two-layer Newtonian viscosity model, where 1 refers to the region closest to the solid surface and the variable β (with associated uncertainty) is the fraction of the total film which is made up of the layer next to the free surface. The particle fractions implied by the viscosities found from the two-layer Newtonian viscosity model are given as ϕ_1 and ϕ_2. The pure liquid viscosity determined as described in the text is given by η_0 in the rightmost column; variation is due to changes in laboratory temperature from day to day. Units of dimensional quantities are indicated in the second line of the top row. The particle radii range from 125 to 150 μm in these experiments.

It is not possible to determine the particle concentration at the free surface precisely from the data obtained here. Due to the relatively small shear stress near the free surface, changes in the effective viscosity at the free surface will result in a very small change in the velocity. Only extremely accurate velocity measurements over the entire film would allow reliable determination of near-surface particle fraction from the velocity profile.

A consideration of the limiting case of the flow down a vertical plane is of some interest. Experiments were done for $\phi_B = 0.3$ and $\alpha = 90°$, but were qualitatively different in behaviour from those at smaller α. For smaller angles of inclination relative to the horizontal a film of very uniform depth in the spanwise direction was obtained, while the film was not uniform in depth at $\alpha = 90°$. In this case of a vertical channel,

most of the flow occurred in the corners between the bottom of the channel and the sidewalls with almost no suspension in the centre of the channel. This behaviour was repeatable and stable to forced disturbances of the free surface. In fact, the flow in the corners is to be expected as shown in the study of film flows in the geometry of the present study by Scholle & Aksel (2003), because our film depth becomes small relative to the capillary length defined $l_c = (2\sigma/\rho g \cos\alpha)^{1/2}$ in the vertical condition (l_c diverges as $\alpha \to 90°$) and Scholle & Aksel have shown that the flow is predominately in the corners under this condition. For $\alpha = 30°$–$70°$ for the other experiments described, we note that $h_o/l_c = O(1)$, and there is minimal influence of the corner flow on the results. Velocimetry measurements were not made for the vertical plane condition.

The film depths, $h(x)$, reported in this study were determined by integrating the particle velocity to find the point where the total material flux was equal to the total flux which was physically set in the experiment. There was close agreement, generally within $100\,\mu\text{m}$, between this and the depth determined by a depth micrometer. We are unable to determine the film depth by integration for the $\phi_B = 0.3$, $\alpha = 90°$ experiment, since our method requires negligible variations in the film thickness in the spanwise direction.

Because of temperature variations, precise reproduction of film thickness proved difficult, and hence results of exact replicates of experiments are not reported. However, the reproducibility of the stereoscopic imaging and velocimetry technique employed in this study is demonstrated in figure 6(a). Two independent camera positionings (setups 1 and 2), with images taken over two different time intervals, were used during the course of a single experiment to measure the velocity profile at $x = 76\,\text{cm}$ ($x/h_o \doteq 290$ for this experiment). Close agreement between the measured velocity profiles in the two intervals is seen. The largest difference in the two trials was $0.08\,\text{mm s}^{-1}$, or $\approx 3\,\%$ of the maximum velocity of $2.85\,\text{mm s}^{-1}$. This supports the significance of the difference in the velocity profiles measured at $x = 15\,\text{cm}$ and $x = 137\,\text{cm}$ from these results. In regard to the reliability of the measurements, note also that the velocities reported in figure 6(c), from experiment 8 at $\phi_B = 0.4$, are within the experimental accuracy identical at $x = 76$ and $137\,\text{cm}$; this indicates not only that this flow was fully developed at the first of these two axial positions, but also that the imaging and velocimetry technique is reliable.

3.2. *Surface imaging*

The surface deformation of a flowing suspension has been characterized by the method described in §2.3. The deformation was studied for experiments in the long channel along with the velocimetry measurements in limited cases, although the great majority were performed in the short channel. Results presented are primarily from these 'initial flow' studies, in which a volume of suspension calculated to produce a film of the desired depth was poured into the short channel in the horizontal position. The suspension was introduced as uniformly as possible to minimize flow during the levelling period. Following this levelling period, the channel was tilted to the inclination angle of interest and images of the surface were captured, with the suspension undergoing a total mean strain of less than 10 ($u_{\max}t/h_o < 10$). Only figure 13 presents results of surface deformation following significant axial flow, with measurements taken at the positions for which velocimetry was performed. The experiments examining the free surface of a uniformly concentrated suspension are summarized in table 2, including a description of the surface observed under our standard magnification.

Exp.	ϕ_B	α deg.	$\bar{a}$ μm	h mm	Ca_p	$h/(2\bar{a})$	Ca_f	Surface Description
1	0.30	34.5	5.0	2.413	1.0×10^{-5}	243.7	2.4×10^{-3}	smooth
2	0.30	34.5	5.0	3.073	1.0×10^{-5}	310.4	3.0×10^{-3}	smooth
3	0.30	0.16	89	1.854	1.2×10^{-5}	11.7	1.4×10^{-4}	smooth
4	0.30	75.6	5.0	2.413	1.6×10^{-5}	243.7	4.0×10^{-3}	smooth
5	0.30	0.48	89	1.854	3.7×10^{-5}	11.7	4.3×10^{-4}	smooth
6	0.30	0.97	89	1.854	7.4×10^{-5}	11.7	8.7×10^{-4}	smooth
7	0.30	1.94	89	1.854	1.4×10^{-4}	11.7	1.7×10^{-3}	deformed
8	0.30	2.86	89	1.854	2.1×10^{-4}	11.7	2.6×10^{-3}	deformed
9	0.30	7.30	89	1.854	5.5×10^{-4}	11.7	6.5×10^{-3}	deformed
10	0.30	7.30	89	13.37	5.5×10^{-4}	84.1	4.7×10^{-2}	deformed
11	0.01	34.6	89	1.981	2.5×10^{-3}	12.5	3.1×10^{-2}	deformed
12	0.05	34.6	89	2.108	2.5×10^{-3}	13.3	3.3×10^{-2}	deformed
13	0.10	34.6	89	2.032	2.5×10^{-3}	12.8	3.2×10^{-2}	deformed
14	0.20	34.5	89	2.337	2.5×10^{-3}	14.7	3.7×10^{-2}	deformed
15	0.20	34.5	89	3.200	2.5×10^{-3}	20.1	5.0×10^{-2}	deformed
16	0.20	34.5	89	4.039	2.5×10^{-3}	25.4	6.3×10^{-2}	deformed
17	0.30	34.5	89	2.134	2.5×10^{-3}	13.4	3.3×10^{-2}	deformed
18	0.30	34.6	89	2.210	2.5×10^{-3}	13.9	3.5×10^{-2}	deformed
19	0.30	34.5	89	3.099	2.5×10^{-3}	19.5	4.9×10^{-2}	deformed
20	0.30	34.5	89	3.912	2.5×10^{-3}	24.6	6.1×10^{-2}	deformed
21	0.30	34.5	89	5.334	2.5×10^{-3}	33.5	8.4×10^{-2}	deformed
22	0.40	34.5	89	2.083	2.5×10^{-3}	13.1	3.3×10^{-2}	deformed
23	0.40	34.5	89	3.048	2.5×10^{-3}	19.2	4.8×10^{-2}	deformed
24	0.40	34.5	89	4.191	2.5×10^{-3}	26.4	6.6×10^{-2}	deformed
25	0.20	60.8	89	2.108	3.8×10^{-3}	13.3	5.1×10^{-2}	deformed
26	0.20	60.8	89	3.124	3.8×10^{-3}	19.6	7.5×10^{-2}	deformed
27	0.20	60.8	89	3.785	3.8×10^{-3}	23.8	9.1×10^{-2}	deformed
28	0.30	60.8	89	2.134	3.8×10^{-3}	13.4	5.2×10^{-2}	deformed
29	0.30	60.8	89	3.048	3.8×10^{-3}	19.2	7.4×10^{-2}	deformed
30	0.30	60.8	89	4.039	3.8×10^{-3}	25.4	9.8×10^{-2}	deformed
31	0.30	60.8	89	5.969	3.8×10^{-3}	37.5	1.4×10^{-1}	deformed
32	0.40	60.8	89	2.057	3.8×10^{-3}	12.9	5.0×10^{-2}	deformed
33	0.40	60.8	89	3.124	3.8×10^{-3}	19.6	7.5×10^{-2}	deformed
34	0.40	60.8	89	4.597	3.8×10^{-3}	28.9	1.1×10^{-1}	deformed
35	0.20	75.0	89	1.854	4.2×10^{-3}	11.7	5.0×10^{-2}	deformed
36	0.20	75.0	89	2.869	4.2×10^{-3}	18.0	7.7×10^{-2}	deformed
37	0.20	75.0	89	4.293	4.2×10^{-3}	27.0	1.2×10^{-1}	deformed
38	0.40	75.0	89	1.823	4.2×10^{-3}	11.5	4.9×10^{-2}	deformed
39	0.40	75.0	89	3.124	4.2×10^{-3}	19.6	8.3×10^{-2}	deformed
40	0.40	75.0	89	4.318	4.2×10^{-3}	27.2	1.2×10^{-1}	deformed
41	0.40	90.0	89	2.083	4.4×10^{-3}	13.1	5.8×10^{-2}	deformed
42	0.40	90.0	89	3.073	4.4×10^{-3}	19.3	8.5×10^{-2}	deformed

TABLE 2. Free-surface characteristics and parameters for all of the uniformly concentrated (or 'initial') free-surface film experiments. The particle size is reported here as the mean radius, $\bar{a}$. The final column indicates whether the image of 2.4 cm × 3 cm showed discernible deformation.

The deformation at the interface reflects a balance between surface tension and viscous stresses, commonly given by a capillary number. Two capillary numbers were considered, the first based on the shear stress averaged over the depth of the film,
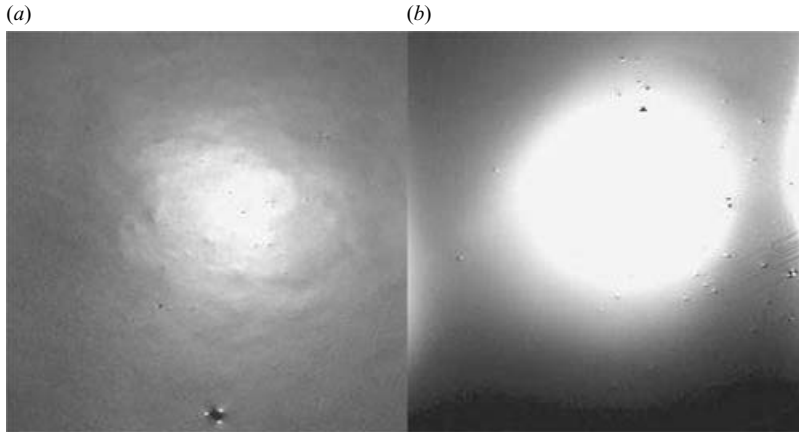
$$Ca_f = \frac{\rho g_x h a}{\sigma},$$

(*a*)   (*b*)

FIGURE 8. Comparison of initial surface topography for films at uniform $\phi = 0.3$. (*a*) $\bar{a} = 89\,\mu\text{m}$, $Ca_f = 2.56 \times 10^{-3}$, and $Ca_p = 2.19 \times 10^{-4}$. (*b*) $\bar{a} = 5.0\,\mu\text{m}$, $Ca_f = 4.02 \times 10^{-3}$, and $Ca_p = 1.65 \times 10^{-5}$. Images are 2.4 cm in width and 3.0 cm in height. The suspension is flowing from top to bottom.

and the second based on the stress at a distance comparable to the particle diameter from the free surface,

$$Ca_p = \frac{2\rho g_x a^2}{\sigma},$$

where σ is the measured surface tension. The former definition, differing by a factor of $1/2$, was used to characterize conditions in computed liquid film flows containing either immiscible liquid drops or rigid particles by Li & Pozrikidis (2002 or 2003, respectively) under fairly dilute conditions. In concentrated suspensions, comparison of surface images indicates that Ca_p provides a better delineation of behaviour than does Ca_f. Experiments conducted at the same bulk solid fraction and same Ca_f but with suspensions of different particle size display different surface topography, as shown in figure 8 for suspensions of $\phi_B = 0.3$; in part (*a*) the suspension is of mean particle radius $\bar{a} = 89\,\mu\text{m}$, while in (*b*) $\bar{a} = 5.0\,\mu\text{m}$. Despite the larger Ca_f in (*b*), the surface shows none of the deformation which is observed in part (*a*), and this was confirmed to be true even at a much higher magnification level for the small-particle suspension. At $Ca_p = 2.2 \times 10^{-4}$ in figure 8(*a*), the surface is deformed by subsurface particles (or groups of particles) while the surface in (*b*), at $Ca_p = 1.7 \times 10^{-5}$, is not noticeably deformed. In general, we find there is a discernible change in surface topography for $\phi_B = 0.3$ at $Ca_p \approx 10^{-4}$.

The relevance of the stress at particle-scale distances from the surface, which is captured by Ca_p, rather than the stress proportional to film depth captured by Ca_f, is also supported by PSD results. Experiments run at the same ϕ_B and inclination angle at varying h_o vary little in wavenumber content of either one- or two-dimensional PSDs, with the former presented in figure 9 for $\phi_B = 0.3$ and $\alpha = 34.6°$.

Dependence of the surface topography on inclination angle (and hence shear stress) and solids fraction is illustrated by figures 10–12. In figure 10, surface images are presented. In the upper group of images (*a–e*), ϕ_B is fixed at 0.3 in a film of $h = 2\,\text{mm}$ (the particle mean radius is 89 µm) and α takes values 0.16°, 2.86°, 7.30°, 34.6°, and 60.8°. The film is not perceptibly deformed at the smallest angle, but is weakly deformed by $\alpha = 2.86°$ and becomes progressively more deformed until
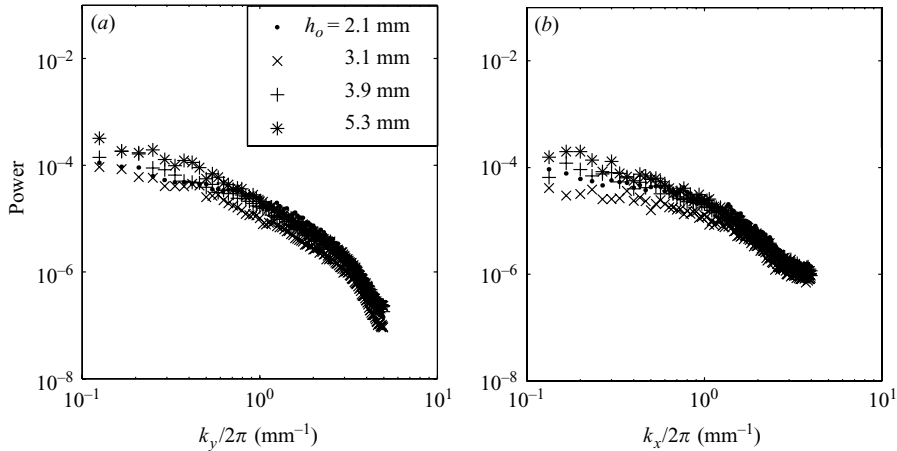
FIGURE 9. Effect of changing film thickness, h_o, on the one-dimensional power spectral densities from surfaces of uniformly concentrated films for $\bar{a} = 89\,\mu\text{m}$, $\phi_\text{B} = 0.3$, and $\alpha = 34.6°$, in (*a*) spanwise direction and (*b*) streamwise direction. These experiments have $Ca_p = 2.5 \times 10^{-3}$ and $Ca_f = 3.5 \times 10^{-2} - 8.4 \times 10^{-2}$.

$\alpha = 34.6°$. There is little change in the deformation when the angle is increased to $\alpha = 60.8°$. In figure 11(*a–e*), the two-dimensional PSDs corresponding to figure 10(*a–e*) show increasing high wavenumber content as α increases, and figure 12 illustrates that the PSD at all but the lowest wavenumbers (which are not presented on the figure) is shifted upward as the surface is progressively inclined. In (*f–j*) of figures 10 and 11, the surface images and two-dimensional PSD are presented for fixed $\alpha = 34.6°$ and $\phi_\text{B} = 0.01$, 0.1, 0.2, 0.3, and 0.4, respectively. Even at the dilute condition of $\phi_\text{B} = 0.01$, surface deformation is visually recognizable, and the PSD shows this deformation to be on a range of scales. As ϕ_B increases, the intensity of the deformation, as well as the relative content in large wavenumbers, is observed to increase. Differences in the surfaces for conditions of $\phi_\text{B} \geqslant 0.2$ are not readily described, but the PSD representation does show differences. Note that in all cases with significant deformation of the interface, the two-dimensional PSD plots show some anisotropy, with larger wavenumbers populated in the flow direction than in the spanwise direction. This may be suggestive of wave formation, but no obvious wave structure is seen; note that the inclined-plane Stokes flow of a thin film of pure liquid should be stable to interfacial waves at $\alpha < 90°$.

The effect of the particle concentration on the surface topography can be seen in figure 10. As the particle fraction increases the surface becomes more deformed, and the relative high-wavenumber content of the surface increases as shown in figure 11.

Recall that the flow develops axially owing to particle migration. It is thus interesting to know the axial dependence of surface topography. While generally similar surface features are seen, a comparison based on the two-dimensional power spectral densities of figure 13 from $x \to 0$, 76 cm, and 137 cm shows differences, the most notable being the appearance of more distinct boundaries between levels in the power at the two downstream locations, and a flattening of the spectrum between the second and third locations, the latter evidenced by the reduction in the range of the power represented in figure 13(*c*).

Low-pass filtering has also been applied to the individual surface images in an attempt to determine the scale of structures within the film resulting in the deformation
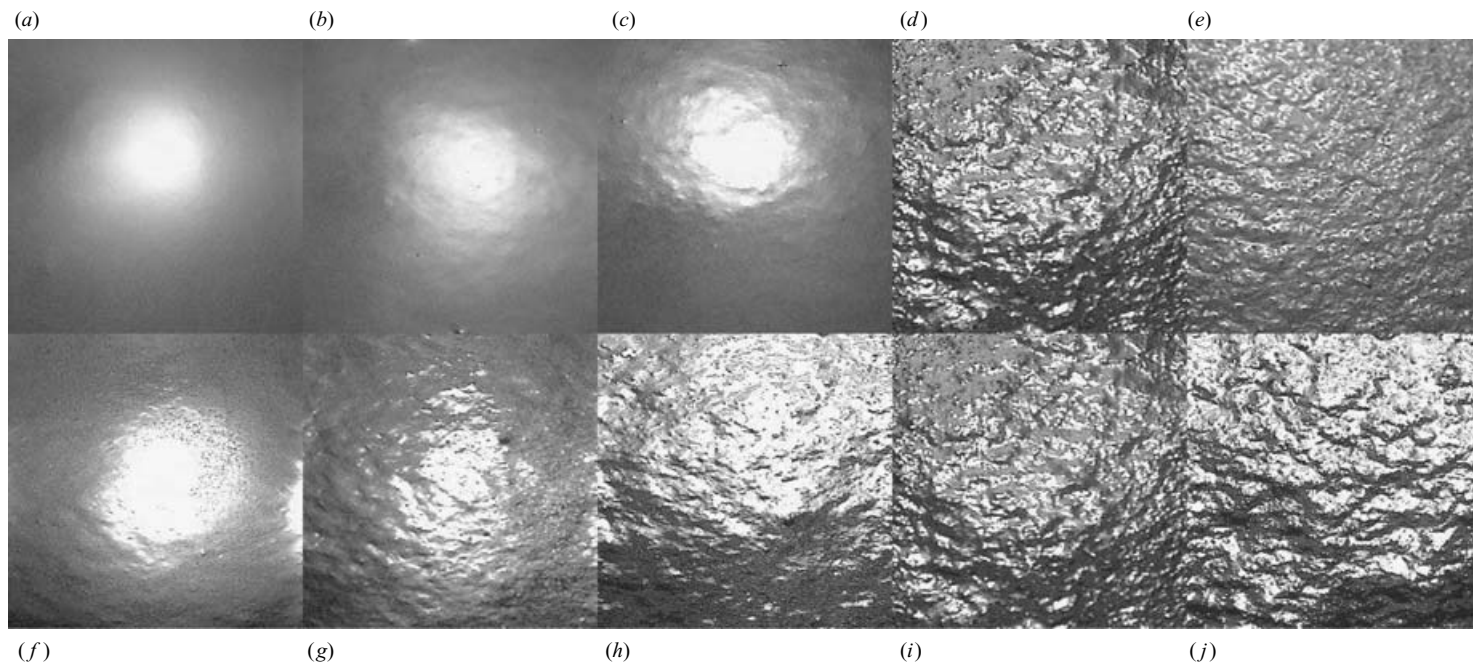
FIGURE 10. Surface images from uniformly concentrated flowing films. Upper row, varying α with $\bar{a} = 89\,\mu\text{m}$, $\phi_B = 0.3$ and $h \approx 2\,\text{mm}$. (a) $\alpha = 0.16°$, (b) $\alpha = 2.86°$ (c), $\alpha = 7.30°$ (d), $\alpha = 34.6°$, and (e) $\alpha = 60.8°$. Lower row, varying ϕ_B with $\bar{a} = 89\,\mu\text{m}$, $\alpha = 34.6°$ and $h \approx 2.0\,\text{mm}$. (f) $\phi_B = 0.01$, (g) $\phi_B = 0.1$, (h) $\phi_B = 0.2$, (i) $\phi_B = 0.3$, and (j) $\phi_B = 0.4$. Images are 2.4 cm wide and 3.0 cm tall. Flow is from the top to bottom in each image.
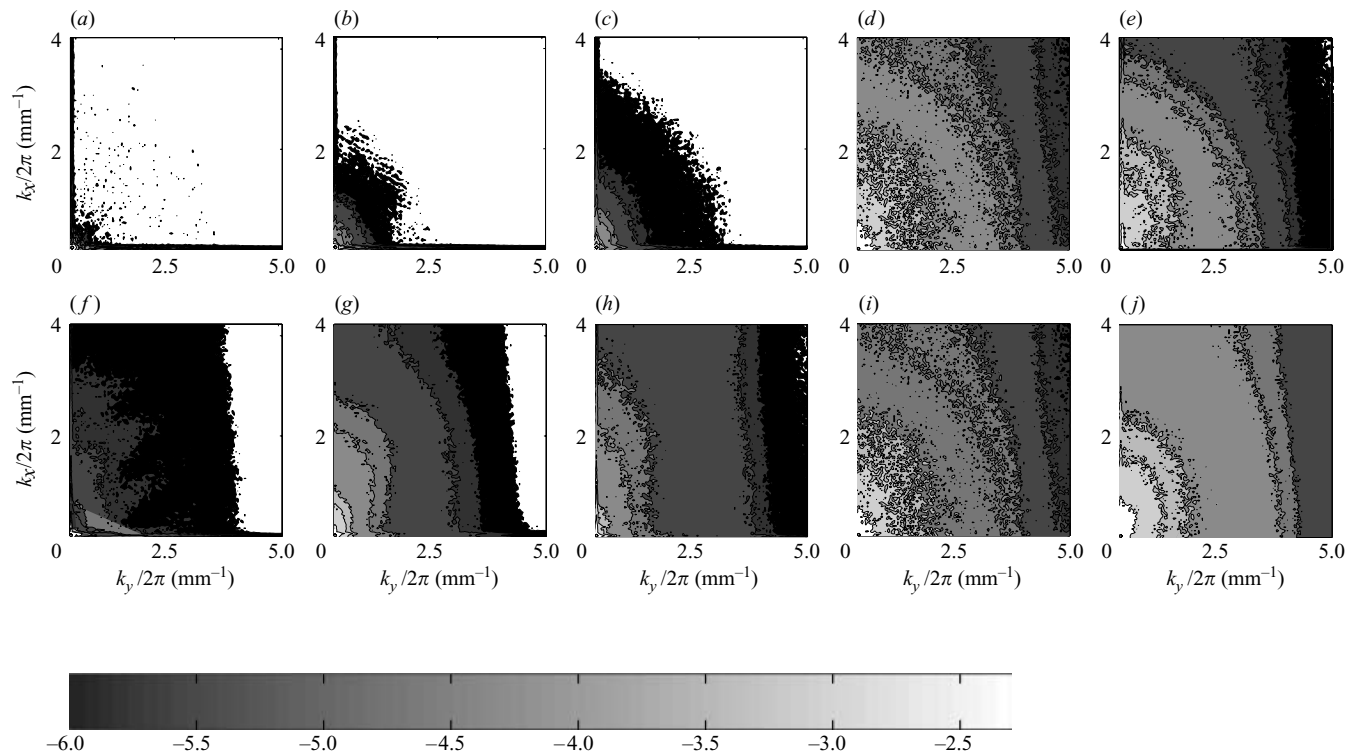
FIGURE 11. Two-dimensional power spectral density for conditions corresponding to figure 10. Upper row, varying α, with $\bar{a} = 89 \, \mu\text{m}$, $\phi_B = 0.3$ and $h_o \approx 2 \, \text{mm}$. (*a*) $\alpha = 0.16°$ (*b*) $\alpha = 2.86°$ (*c*) $\alpha = 7.30°$ (*d*) $\alpha = 34.6°$ (*e*) $\alpha = 60.8°$. Lower row, varying ϕ_B with $\bar{a} = 89 \, \mu\text{m}$, $\alpha = 34.6°$ and $h_o \approx 2.0 \, \text{mm}$. (*f*) $\phi_B = 0.01$, (*g*) $\phi_B = 0.1$, (*h*) $\phi_B = 0.2$, (*i*) $\phi_B = 0.3$, and (*j*) $\phi_B = 0.4$. The values plotted are $\log_{10}$ of the power, with the mapping to grey scale indicated in the bar. The large regions of white space in the high wavenumber region represent powers which are smaller than 10^{-6}.
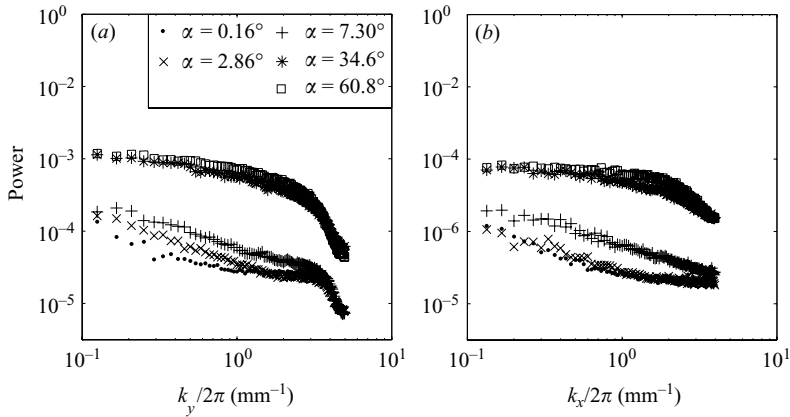
FIGURE 12. One-dimensional power spectral density from surfaces of uniformly concentrated films flowing at varying α with $\bar{a} = 89\,\mu\text{m}$, $\phi = 0.3$, and $h_o \approx 2\,\text{mm}$ in (a) spanwise direction, and (b) downstream direction.
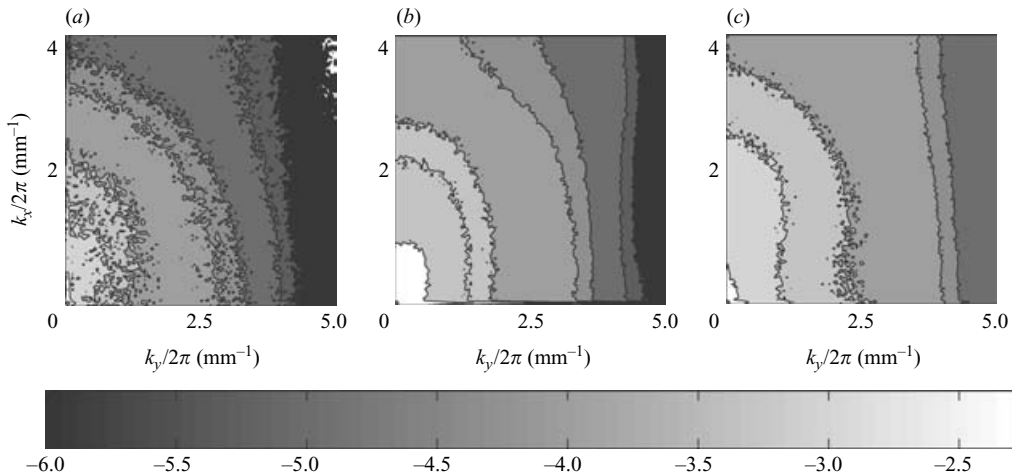

FIGURE 13. Two-dimensional power spectral density for different axial locations, with $2\bar{a} = 89\,\mu\text{m}$, $\phi_B = 0.3$, $\alpha = 60.8°$, and $h_o = 2.1\,\text{mm}$. (a) Initial surface, $x \to 0$, (b) $x = 76\,\text{cm}$, and (c) $x = 137\,\text{cm}$. The values plotted are $\log_{10}$ of the power. A mapping to grey scale is shown in the bar.

of the interface. Low-pass filtering was done with cutoff wavenumbers (wavelengths, λ) of $1.2\,\text{mm}^{-1}$ ($\lambda = 5.3\,\text{mm}$), $2.6\,\text{mm}^{-1}$ ($\lambda = 2.4\,\text{mm}$), $4.2\,\text{mm}^{-1}$ ($\lambda = 1.5\,\text{mm}$), $12.6\,\text{mm}^{-1}$ ($\lambda = 0.5\,\text{mm}$), and $20.9\,\text{mm}^{-1}$ ($\lambda = 0.3\,\text{mm}$), where all wavenumbers which were larger than these were discarded. Examples of these filtered images can be seen in figure 14. When the filtered images are viewed in video form (as a time series), structures associated with all wavenumbers are observed to move downstream.

4. Flow modelling

Gravity-driven Stokes flow of a film of Newtonian fluid down an inclined plane results in a quadratic velocity profile. The standard assumption of vanishing shear stress at the gas–liquid interface, or free surface, results in a flow mathematically
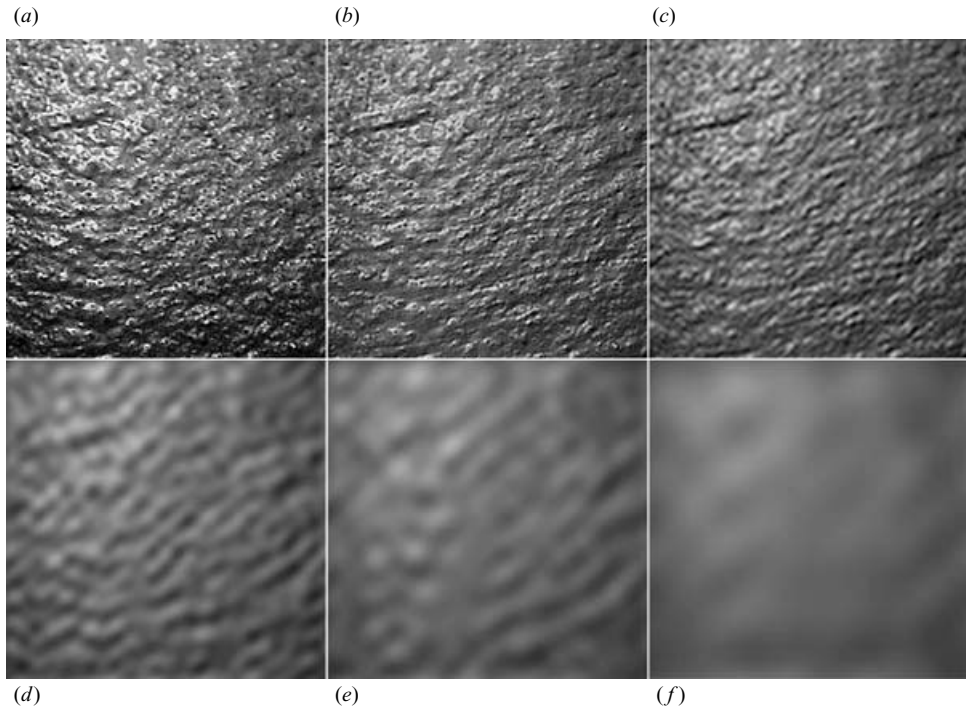
FIGURE 14. Filtered surface images from a uniformly concentrated film, with $\bar{a} = 89\,\mu\text{m}$, $\phi_B = 0.3$, $\alpha = 60.8°$, and $h_o = 2.1\,\text{mm}$: (a) Original image; (b) largest wavenumber of $20.9\,\text{mm}^{-1}$ ($\lambda = 0.3\,\text{mm}$), (c) $12.6\,\text{mm}^{-1}$ ($\lambda = 0.5\,\text{mm}$), (d) $4.2\,\text{mm}^{-1}$ ($\lambda = 1.5\,\text{mm}$), (e) $2.6\,\text{mm}^{-1}$ ($\lambda = 2.4\,\text{mm}$), and (f) $1.2\,\text{mm}^{-1}$ ($\lambda = 5.3\,\text{mm}$). Images are 2.4 cm wide and 3.0 cm tall. Flow is from the op of the each image toward the bottom.

identical to pressure-driven channel, or plane Poiseuille, flow with the gravitational driving force replacing the gradient of pressure, of form $u(\xi) = U_s[1 - (\xi/h)^2]$ where ξ is measured from the free surface into the liquid ($\xi = h - z$), U_s is the surface velocity and h is the film depth. Suspensions of neutrally buoyant particles in pressure-driven channel flow exhibit shear-induced migration, with elevated concentration developing in the centre of the channel as the flow proceeds axially. It is thus natural to apply modelling successful for predicting migration phenomena in pressure-driven and other flows to the study of gravity-driven suspension film flow. The model we use is based on the suspension balance approach of Nott & Brady (1994) with the different description of the normal stress rheology proposed in Morris & Boulay (1999).

The new features considered here are the potential for a normal stress jump across the free surface and the free-boundary character of the upper surface of the film. The latter allows the mean film depth to vary as the mixture flows axially, and thus provides the capability to match the experimentally observed thinning of the film, as shown by the $h(x)$ data in table 1. The mean free surface is nearly flat, and thus takes on too weak a curvature to be of significant influence under the conditions studied, but the possibility for a normal stress jump resulting from the smaller-scale fluctuating deformations of the free surface of the suspension is addressed below.

We consider flows in which the film-scale inertia and the particle-scale inertia are small, justifying neglect of inertia at all scales. In the suspension balance approach, neutrally buoyant suspension flow at zero Reynolds number is described by mass and

momentum conservation equations for the bulk mixture and for the particle phase. The bulk balances are

$$\nabla \cdot \langle \boldsymbol{u} \rangle = 0 \quad \text{and} \quad \nabla \cdot \boldsymbol{\Sigma} + \rho \boldsymbol{g} = 0, \tag{4.1}$$

with the mean suspension velocity and bulk stress given by $\langle \boldsymbol{u} \rangle$ and $\boldsymbol{\Sigma}$, respectively. Particle mass conservation is described by

$$\frac{\partial \phi}{\partial t} + \langle \boldsymbol{u} \rangle \cdot \nabla \phi = -\nabla \cdot \boldsymbol{j}, \tag{4.2}$$

in which $\boldsymbol{j} \equiv \phi(\boldsymbol{U} - \langle \boldsymbol{u} \rangle)$ is the particle flux relative to the mean motion, with $\boldsymbol{U}$ the mean velocity of the particle phase, which is governed by

$$0 = \nabla \cdot \boldsymbol{\Sigma}_p - \frac{9\eta_0}{2a^2} \phi f^{-1}(\phi)(\boldsymbol{U} - \langle \boldsymbol{u} \rangle), \tag{4.3}$$

for neutrally buoyant particles; it was shown in Morris & Brady (1998) that only the difference in density $\rho_p - \rho_f$ enters this equation. The last term on the right of (4.3) represents the hydrodynamic force on the particle phase due to its motion relative to the bulk average velocity, and thus is represented as analogous to a sedimentation with f the sedimentation hindrance function. The particle contribution to the bulk stress, $\boldsymbol{\Sigma}_p$, is modelled as

$$\boldsymbol{\Sigma}_p = -\eta_0 \dot{\gamma} \boldsymbol{Q}(\phi) + 2\eta_0 \eta_p(\phi) \boldsymbol{E}, \tag{4.4}$$

where η_p is the dimensionless particle contribution to the suspension viscosity, and $\boldsymbol{E}$ is the local bulk rate of strain, $\dot{\gamma} = (2\boldsymbol{E} : \boldsymbol{E})^{1/2}$. The normal stresses are specified by the dimensionless material property tensor $\boldsymbol{Q}$, which is taken to be

$$\boldsymbol{Q}(\phi) = \eta_n(\phi) \begin{pmatrix} 1 & 0 & 0 \\ 0 & \lambda_2 & 0 \\ 0 & 0 & \lambda_3 \end{pmatrix} \equiv \eta_n(\phi) \hat{\boldsymbol{Q}}, \tag{4.5}$$

where $\eta_n(\phi)$ is termed the 'normal stress viscosity'. The sedimentation hindrance function, f, relates the sedimentation rate of a homogeneous suspension of spheres at volume fraction ϕ to the isolated Stokes settling velocity, i.e., $f(\phi) = U_{sed}(\phi)/U_{sed}(0)$. A standard form, $f(\phi) = (1-\phi)^\alpha$, is used here (Richardson & Zaki 1954) with $\alpha = 4$. The anisotropy of the stress is given by $\lambda_{2,3}$ differing from unity, with values of $\lambda_2 = 0.5$ and $\lambda_3 = 0.8$ providing best fits of various suspension flows. It is important to note that the vorticity direction is in the 2 position and the gradient in the 3 position, which is unusual (and differs from the original work). Here, we are interested only in the z-directed normal stress but have provided the full constitutive behaviour described by Morris & Boulay (1999) for completeness. Particle contributions to shear and normal stress were treated empirically as

$$\eta_p = 2.5\eta_0 \frac{\phi}{\phi_{\max}} \left(1 - \frac{\phi}{\phi_{\max}} \right)^{-1} + K_s \eta_0 \left(\frac{\phi}{\phi_{\max}} \right)^2 \left(1 - \frac{\phi}{\phi_{\max}} \right)^{-2}, \tag{4.6}$$

$$\eta_n = K_n \eta_0 \left(\frac{\phi}{\phi_{\max}} \right)^2 \left(1 - \frac{\phi}{\phi_{\max}} \right)^{-2}, \tag{4.7}$$

where $K_s = 0.1$ and $K_n = 0.75$ provided reasonable agreement with experimental data. The maximum packing fraction of $\phi_{\max} = 0.65$ is slightly different than in Morris & Boulay.

The problem studied is steady in average but axially varying, and variations of stresses in the axial direction are much smaller than those across the channel. These features reduce the governing equation for $\phi(x, z)$ to

$$\langle u_x \rangle \frac{\partial \phi}{\partial x} = -\frac{\partial j_z}{\partial z} = -\frac{2a^2}{9\eta_0} \frac{\partial}{\partial z} \left(f(\phi) \frac{\partial \Sigma_{zz}^P}{\partial z} \right) \tag{4.8}$$

in which it is assumed that the average mixture velocity has only an axial component in writing the left-hand side. Note that z in this problem is the direction of the velocity variation, or the gradient direction, and thus $\Sigma_{zz}^P = \Sigma_{33}^P$. The boundary conditions associated with (4.8) are that no particle flux occurs through either the solid boundary or the free surface; we require constant axial flux of both particles and bulk suspension at any value of x, which condition is related to the determination of the free-surface position (i.e. to the value of $h(x)$).

We assume that the particles move with the mean suspension velocity in the axial direction, neglecting the lag velocity of $O[(a/h)^2]$ predicted by Faxén's law. The solution is obtained using a marching method described by Miller & Morris (2003), such that the axial momentum equation uses only local information, meaning values at the axial position x of interest,

$$0 = \rho g \sin \alpha + \frac{\partial}{\partial z} \left(\eta_s(\phi) \frac{\partial u_x}{\partial z} \right) \tag{4.9}$$

and from this we determine u_x and $\dot{\gamma} = \partial u_x / \partial z$. This information, along with the profile $\phi(z)$ at this x, is used to evaluate Σ_{zz}^P and its variation with z, and hence the cross-stream particle flux due to particle migration, j_z. This leads to an updated equation for ϕ which, following from (4.8), yields

$$\Delta \phi = -\frac{\Delta x}{u_x(z)} \frac{\partial j_z}{\partial z} = -\frac{2a^2 \Delta x}{9\eta_0 u_x(z)} \frac{\partial}{\partial z} \left(f \frac{\partial \Sigma_{zz}^P}{\partial z} \right). \tag{4.10}$$

In order to apply the model to the film flow, a boundary condition for the free surface must be developed. Considering the local conditions at a free surface, a normal stress jump is admitted across the interface, and a finite normal stress at the interface is needed for a fully developed solution satisfying the condition $\partial \Sigma_{zz}^P / \partial z = 0$ to apply, given the rheological model of the mixture; this is similar to the need for a finite normal stress at the centreline of fully developed pressure-driven flow captured in different ways in Nott & Brady (1994) and Frank *et al.* (2003). Despite the necessity of some normal stress at the interface owing to this 'solvability condition' for the flow, this jump has little effect aside from keeping the free-surface value of ϕ below maximum packing until it is made comparable to the mean film shear stress. The normal stress jump at the free surface is set as follows:

$$\Sigma_{zz}^P = \Sigma_{zz(o)}^P - C \eta_0 \eta_n \frac{\overline{u_x}}{h}$$

where η_n is the normal stress viscosity at the local value of ϕ, and $\Sigma_{zz(o)}^P \sim -\eta_n \dot{\gamma}$ is the locally calculated particle stress and thus vanishes at the free surface, where $\dot{\gamma} = 0$. The second term on the right of the above expression is thus the non-local portion of the particle stress, which causes a normal stress jump at the free surface. The parameter C was varied from 0.001 to 10, with values of $C = (0.001, 0.01, 0.1, 1, 2, 10)$ yielding $h/h_o = (0.842, 0.847, 0.852, 0.903, 0.980, 0.997)$, respectively: migration is significantly reduced only for values of $C \geqslant 1$, with little difference in the velocity and concentration profiles for $C = 0.001$ to 0.1. The fully developed dimensionless film thickness is closest
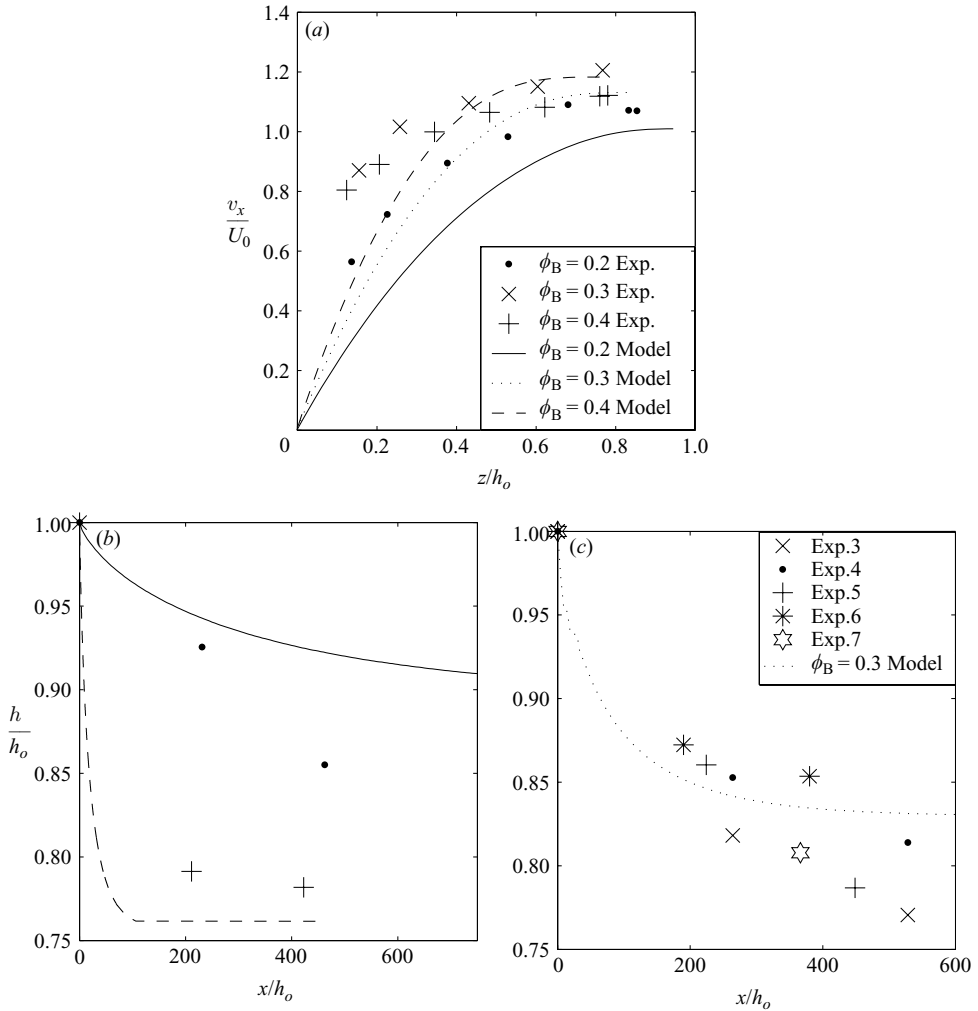
FIGURE 15. (*a*) Comparison of dimensionless velocity profiles determined experimentally at $x = 137$ cm with the fully developed model velocity profiles. Comparison of model predictions of film thickness and experimentally determined film thickness for (*b*) $\phi_B = 0.2$ and 0.4, and (*c*) $\phi_B = 0.3$. The experimental data for $\phi_B = 0.2$, 0.3, and 0.4 were taken from Experiments 2, 3 and 8, respectively, as labelled in table 1. The model parameter value of $C = 0.1$ is used. The legend in (*a*) applies also to (*b*).

to the experimentally determined result for values of $C \leqslant 0.1$, and further modelling predictions presented use $C = 0.1$.

Model predictions for velocity and film depth are compared with the experimental observations for $\phi_B = 0.2$, 0.3, and 0.4 in figure 15. The observed shear rate at the wall is large relative to the predictions. The model does not predict that ϕ will approach zero at the wall, as observed in the experiments. The predictions of the evolving film depth are in reasonable agreement with the model predictions for the two higher solids fractions, but for $\phi_B = 0.2$ the experimental evolution is both more rapid and more extreme (the predicted asymptote for $\phi_B = 0.2$ is $h/h_o \doteq 0.89$ and the observed value h/h_o at the last measurement location is below this value). The discrepancy
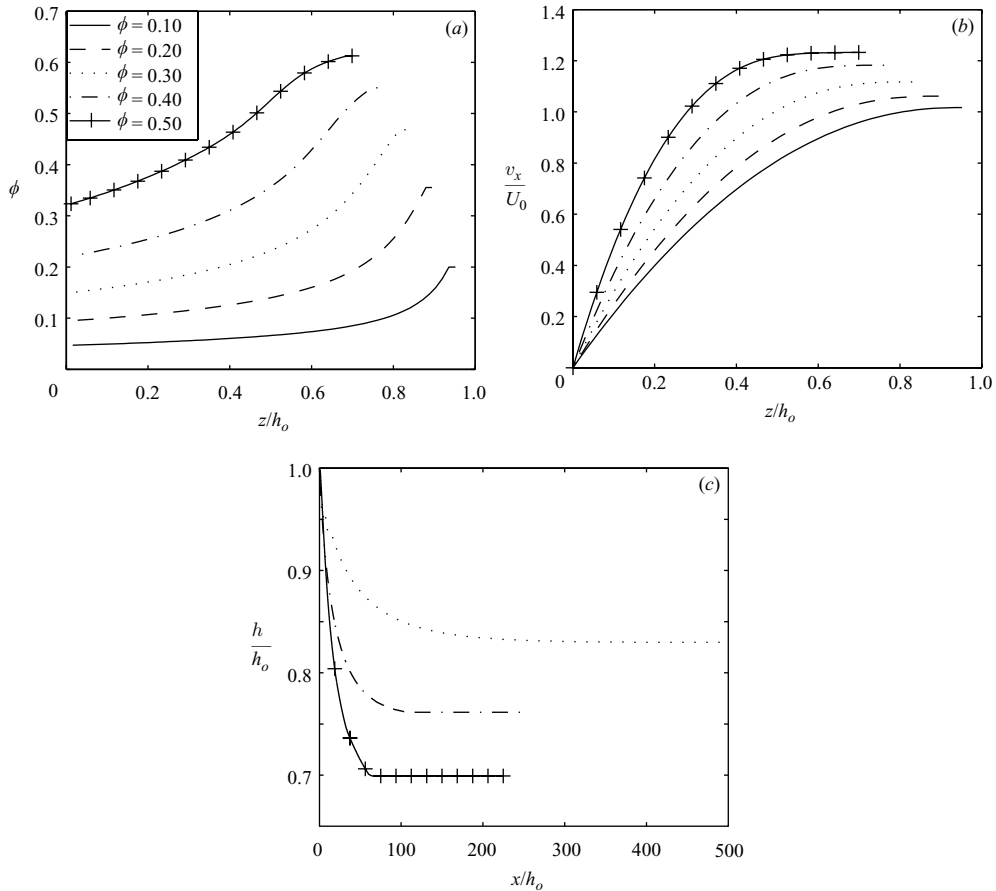
FIGURE 16. Model solutions for various ϕ_B with $C = 0.1$: (a) ϕ profile, (b) velocity profiles, and (c) evolution of h/h_o. The fully developed states based on h/h_o for $\phi_B = 0.1$ and 0.2 occurs at $x/h_o \approx 10\,000$ and 2800, respectively, and curves for these conditions are omitted from (c).

appears to be related again to the model failure to predict the rapid drop of ϕ toward zero adjacent to the solid boundary.

To give a more complete view of the model for a range of conditions, velocity and concentration profiles and the axial evolution predicted for $0.1 \leqslant \phi_B \leqslant 0.5$ are presented in figure 16. The scaled film depth is predicted to decrease and the scaled surface velocity to increase with increasing ϕ. The model predictions of the axial evolution of h/h_o for different ϕ_B are presented in figure 16(c), and are of interest for interpretation of the experimental results. The predictions for $\phi_B = 0.1$ and 0.2 are that the depth continues to decrease slowly until $x/h_o = 10\,000$ and 2800, respectively, and are omitted from the plot. This long development length for $\phi_B = 0.2$ suggests strongly that the flow experiment 2, as labelled in table 1, is not fully developed, although the discrepancy between model and experiment noted just above should also be borne in mind.

5. Discussion and conclusions

Experiments from this study have shown that particle migration in gravity-driven suspension film flow occurs under a range of conditions, and that the shear-stress-free

surface of the film becomes deformed over a range of scales. The conditions studied were highly viscous, as $Re_f \ll 1$. In general, the films studied were relatively thin in the sense that they are of $O(10)$ particle diameters in depth. Velocity profiles determined by stereoscopic imaging and particle correlation velocimetry have shown, for all suspensions of $\phi_B \geqslant 0.2$ studied, a decrease in effective viscosity of the material nearest the wall as the suspension moves down the inclined plane, implying a reduction in ϕ here. The added shear rate due to this migration away from the wall causes the velocity near the wall to increase above its value for the uniform suspension. The mean flow is observed to be steady and this increased shear rate leads to a decrease in film thickness to maintain constant material flux. These results agree with predictions from the suspension balance model in the form proposed by Morris & Boulay (1999).

There is insufficient information from our experiments to make conclusive statements about the particle concentration next to the free surface, but the comparisons of experiment and model results lead us to believe the model overpredicts ϕ adjacent to the interface. The model has not included a mechanistic description of the influence of the interface, although a non-local stress contribution has been used to provide a finite normal stress jump across the position of the mean interface. That the interface, despite being essentially flat in the mean, could provide a balancing stress to a finite particle normal stress is quite reasonable, as it becomes highly deformed, i.e. the root mean square curvature is certainly non-zero. As argued in Loimer *et al.* (2002), who observed such deformations at the upper surface (in the vorticity direction) of a simple shear flow driven by vertical belts, such deformations may result in a net force upon the particle phase. It is worthwhile to note in considering such a possibility that for such a situation to hold in a steady state, if the particles are pushed into the film, the liquid must be subjected to the opposite force and would be pulled into the vicinity of the interface.

What is suggested above is that the film interface serves to balance the driving force for migration of the particle phase predicted by model and expected based on the similarity of the flow with the well-studied pressure-driven channel flow. There is further support from simulation of two-dimensional gravity-driven film flow containing drops and particles by Li & Pozrikidis (2002, 2003). These boundary-integral technique calculations show that in this flow, a single rigid particle is driven away from the free surface as a result of the particle-induced flow causing a nonlinear interaction in deforming the free surface; the work further shows that there is a noticable depletion of drops, present at a bulk areal fraction of 0.2, adjacent to the interface. Detailed comparisons of our results with this work are not readily performed as velocity data are not presented.

Boundary conditions are needed to complete any analysis of a flow, and the same is true of mixture flows. Suspension flows have been intensively modelled, but the boundary conditions remain somewhat less well-understood than the migration phenomena which have in many cases motivated the modelling studies. The capacity of the interface to discriminate between phases illustrated here and in the numerical work noted just above leads us to conclude that this problem must be taken up by techniques employed in mixture flow analysis, wherein an ensemble averaging technique is applied. It is expected that simulation could aid in such developments.

The gravity-driven suspension film flow differs quite significantly from its Newtonian counterpart because of migration effects and surface deformation, and also from the seemingly similar pressure-driven flow of a suspension in a rectangular channel. While the latter flow is an imperfect analogue, the expectations of migration and surface deformation due to suspension normal stresses derived from consideration of this

flow certainly hold. We may safely conclude from our study that suspension normal stresses are finite even at a boundary where the shear stress vanishes. This supports the concept of non-local normal stress modelling which has been proposed for such flows, using the suspension temperature modelling (Nott & Brady 1994; Morris & Brady 1998) or simpler approaches not requiring an additional field variable as in the model employed here (Morris & Boulay 1999). The proper form of these non-local stresses remains, however, an open question.

Appendix. Stereoscopic image analysis

The transformation from the captured two-dimensional image to a position in three-dimensional space employed in the stereoscopic particle positioning outlined in § 2.2 is described here. The x- and y-coordinates in physical space are defined by the three points which lie in the plane, and in practice were always oriented such that the positive x-coordinate corresponds to the long axis of the channel (the mean flow direction) and the y-coordinate corresponds to the spanwise direction. The z-coordinate is defined using the out-of-plane point, and is zero at the solid surface and positive above it.

The lens system used consisted of a series of thin lenses. It can thus be assumed that all of the vectors going to the camera are parallel, as verified experimentally after the fact as described in § 2.2. Because the vectors are essentially parallel, we are able to develop a linear transformation between the location at which each vector intersects the $z = 0$ plane in three-space and the two-dimensional coordinate system of the image from the camera (Born & Wolf 1999). This transformation is of the following form:

$$X = T \cdot w + R, \tag{A 1}$$

where X is a position where this particular vector intersects the (x, y)-plane $(z = 0)$, w is the position of the object in the image space taken by the camera, T is a two by two matrix, and R is a vector of length two. Once the three points in the (x, y)-plane have been located in the coordinate system of the image, the matrix T and the vector R are then determined by solving (A 1), or more explicitly:

$$T = A \cdot B \tag{A 2}$$
$$R = -T \cdot d_1 - c_1. \tag{A 3}$$

Quantities in (A 2) and (A 3) are defined as follows: the columns of A are given by $c_2 - c_1$ and $c_3 - c_1$ respectively, with c_i a column vector denoting the location of object i in the physical (x, y) plane; the columns of B are given by $d_2 - d_1$ and $d_3 - d_1$ respectively, where d_i is a column vector denoting the location of object i in the image (V, W) space, a subscript 1 denotes the object being used as the physical space origin, and subscripts 2 and 3 denote the physical space objects which define the x- and y-axes in physical space. The caption gives the image space and corresponding physical space location of the points identified in figure 2. The three points with a z position of 0.00 are used to determine T and R for this camera. The image space coordinate system (V, W) is defined with $(0, 0)$ at the top left corner of the picture and is illustrated in figure 2. It is necessary to determine the direction

associated with the vectors from each camera. Under the approximation of parallel vectors from the image to the camera, the direction in which the camera must be from all objects which are observed can be determined from the identifiable point on the optical standard which lies out of the $(x, y, z = 0)$ plane. This is the point located at $(V = 198, W = 97)$ in the example of figure 2. The relation (A 1) is used to determine the point where the vector from the out-of-plane point to the camera intersects the $(x, y, z = 0)$ plane. The direction in which the camera lies from all viewable objects is defined by the difference between the actual position of the out-of-plane identifiable point of the optical standard and the point determined from (A 1) above, given the (V, W) coordinates of the out-of-plane point.

The vector along which a point on an object lies is defined by the point at which the ray of light intersects the $(x, y, z = 0)$ plane, which is found using (A 1), and the direction associated with the camera, found by the procedure outlined in the previous paragraph. Recall that a vector to a point is determined for each camera, and a line along the vector direction can be defined for each. The three-dimensional location of an observed object is the point where the lines associated with that object from the two cameras intersect. In practice, the object position is taken as the point which minimizes the sum of the distances between itself and each vector. This point bisects the shortest possible line between the two vectors.

REFERENCES

ABBOTT, J. R., TETLOW, N., GRAHAM, A. L., ALTOBELLI, S. A., FUKUSHIMA, E., MONDY, L. A. & STEPHENS, T. S. 1991 Experimental observations of particle migration in concentrated suspensions: Couette flow. *J. Rheol.* **35**, 773.

AVERBAKH, A., SHAULY, A., NIR, A. & SEMIAT, R. 1997 Slow viscous flows of highly concentrated suspensions—Part I: Laser-Doppler velocimetry in rectangular ducts. *Intl J. Multiphase Flow* **23**, 409.

BOOTE, O. A. M. & THOMAS, P. J. 1999 Effects of granular additives on transition boundaries between flow states of rimming flows. *Phys. Fluids* **11**, 2020.

BORN, M. & WOLF, E. 1999 *Principles of Optics: Electromagnetic Theory of Propagation, Interference and Diffraction of Light*, 7th Edn. Cambridge University Press.

BREEDVELD, V., VAN DEN ENDE, D., TRIPATHI, A. & ACRIVOS, A. 1998 The measurement of the shear-induced particle and fluid tracer diffusivities in concentrated suspensions by a novel method. *J. Fluid Mech.* **375**, 297.

FRANK, M., ANDERSON, D., WEEKS, E. A. & MORRIS, J. F. 2003 Particle migration in pressure-driven flow of a Brownian suspension. *J. Fluid Mech.* **493**, 363.

KOH, C. J., HOOKHAM, P. & LEAL, L. G. 1994 Experimental investigation of concentrated suspension flows in a rectangular channel. *J. Fluid Mech.* **266**, 1.

LEIGHTON, D. T. & ACRIVOS, A. 1987 The shear-induced migration of particles in concentrated suspensions. *J. Fluid Mech.* **181**, 415.

LEPOUTRE, P. & LORD, D. 1990 Destabilized clay suspensions: Flow curves and dry film properties. *J. Colloid Interface Sci.* **134**, 66.

LI, X. & POZRIKIDIS, C. 2000 Wall-bounded shear flow and channel flow of suspensions of liquid drops. *Intl J. Multiphase Flow* **26**, 1247.

LI, X. & POZRIKIDIS, C. 2002 Film flow of a suspension of liquid drops. *Phys. Fluids* **14**, 61.

LI, X. & POZRIKIDIS, C. 2003 Film flow of suspension down an inclined plane. *Phil. Trans. R. Soc. Lond.* A **361**, 847.

LI, Y. 1992 Reforming the theory of invariant moments for pattern recognition. *Pattern Recognition* **25**(7), 723.

LOIMER, T., NIR, A. & SEMIAT, R. 2002 Shear-induced corrugation of free interfaces in concentrated suspensions. *J. Non-Newtonian Fluid Mech.* **102**, 115.

LYON, M. K. & LEAL, L. G. 1998 Experimental study of the motion of concentrated suspensions in two-dimensional channel flow. Part 1. Monodisperse systems. *J. Fluid Mech.* **363**, 25.

MILLER, R. M. & MORRIS, J. F. 2003 Development of a frame-invariant suspension flow model. In *Computational Methods in Multiphase Flow* (ed. A. A. Mammoli & C. A. Brebbia). Wessex Institute Press.

MORRIS, J. F. & BOULAY, F. 1999 Curvilinear flows of noncolloidal suspensions: The role of normal stresses. *J. Rheol.* **43**, 1213.

MORRIS, J. F. & BRADY, J. F. 1998 Pressure-driven flow of a suspension: Buoyancy effects. *Intl J. Multiphase Flow* **24**, 105.

NELDER, J. A. & MEAD, R. 1965 A simplex method for function minimization. *Comput. J.* **7**, 308.

NOTT, P. R. & BRADY, J. F. 1994 Pressure-driven flow of suspensions: simulation and theory. *J. Fluid Mech.* **275**, 157.

PHILLIPS, R. J., ARMSTRONG, R. C., BROWN, R. A., GRAHAM, A. & ABBOTT, J. R. 1992 A constitutive model for concentrated suspensions that accounts for shear-induced particle migration. *Phys. Fluids* **4**, 31.

PRASAD, A. K. 2000 Stereoscopic particle image velocimetry. *Exps. Fluids* **29**, 103.

PRANCKH, F. R. & SCRIVEN, L. E. 1990 Elastohydrodynamics of blade coating. *AICHE J.* **36**, 587.

RICHARDSON, J. F. & ZAKI, W. N. 1954 Sedimentation and fluidization. Part I. *Trans. Inst. Chem. Engrs.* **32**, 35.

SCHOLLE, M. & AKSEL, N. 2003 Thin film limit and film rupture of the visco-capillary gravity-driven channel flow. *Z. Angew. Math. Phys.* **54**, 517.

SHAULY, A., AVERBAKH, A., NIR, A. & SEMIAT, R. 1997 Slow viscous flows of highly concentrated suspensions—Part II: Particle migration, velocity and concentration profiles in rectangular ducts. *Intl J. Multiphase Flow* **23**, 613.

TIMBERLAKE, B. D. & MORRIS, J. F. 2002 Concentration band dynamics in free-surface Couette flow of a suspension. *Phys. Fluids* **14**, 1580.

TIMBERLAKE, B. D. & MORRIS, J. F. 2003 Film depth and concentration banding in free-surface Couette flow of a suspension. *Phil. Trans. R. Soc. Lond.* A **361**, 895.

TIRUMKUDULU, M., MILEO, A. & ACRIVOS, A. 2000 Particle segregation in monodisperse sheared suspensions in a partially filled rotating horizontal cylinder. *Phys. Fluids* **12**, 1615.

TIRUMKUDULU, M., TRIPATHI, A. & ACRIVOS, A. 1999 Particle segregation in monodisperse sheared suspensions. *Phys. Fluids* **11**, 507.

WATSON, D. B. 1996 Time lags in the impulse voltage breakdown of PMMA at high temperatures. *J. Phys.* D: *Appl. Phys.* **29**, 3129.

WESTERWEEL, J. 1998 Fundamentals of digital particle image velocimetry. *Meas. Sci. Technol.* **8**, 1379.

ZARRAGA, I. E., HILL, D. A. & LEIGHTON, D. T. 2000 The characterization of the total stress of concentrated suspensions of noncolloidal spheres in Newtonian fluids. *J. Rheol.* **44**, 185.